Coherent noise sources of a subsonic round jet investigated using hydrodynamic and acoustic phased-microphone arrays

Takao Suzuki†

Acoustics & Fluid Mechanics, The Boeing Company, Seattle, WA 98124-2207, USA

Based on phased-microphone array data acquired in the past, properties of coherent noise sources in a subsonic round jet are investigated at low frequencies ($0.2 \lesssim St \lesssim 0.6$) via two approaches: (i) by extracting hydrodynamic fluctuations from the near-field array, instability-wave components are projected to the acoustic field using a boundary-value problem technique; (ii) by post-processing mid-field array data in an acoustic field, noise sources are decomposed into multipole distributions using a generalized-inverse beam-forming technique. Comparison between the projected acoustic fields from the hydrodynamic array and the sound pressure levels at the acoustic array implies that the near-field pressure fluctuations beyond the end of the potential core primarily contribute to the downstream sound, as mentioned by many previous studies. However, the jet-spreading effect, which creates the streamwise growth and decay of the eigenfunctions in linear stability analysis, is insufficient to generate the sound pressure levels measured in the acoustic array. In the actual hydrodynamic data, the streamwise decay is much slower and the phase velocity is faster than those of the corresponding eigenfunction beyond the peak of the wave-packet, and these factors govern the downstream sound. Results from the acoustic array demonstrate that free-space multipole distributions detected by generalized-inverse beam-forming can reproduce primary coherent modes, the first one predominantly propagating downstream and the second one typically being more omni-directional. In particular, the detected phase relation of the first coherent mode shows nearly a constant slope, indicating a wavy-type source structure and the relation of downstream sound with instability waves.

Key words: acoustics, aeroacoustics, jet noise

1. Introduction

Since Lighthill (1952) proposed a sound-generation mechanism by turbulence, many researchers have attempted to validate/invalidate his theory by applying it to jet noise with necessary modifications and to seek its source representations, as cited below. It is fair to state, however, that the noise-source representation of subsonically convecting jets (i.e. the convective velocity of disturbances in the shear layer is subsonic) remains

† Former address: Graduate School of Engineering, University of Fukui, 3-9-1 Bunkyo, Fukui, 910-8507, Japan. Email address for correspondence: takao.seattle@gmail.com
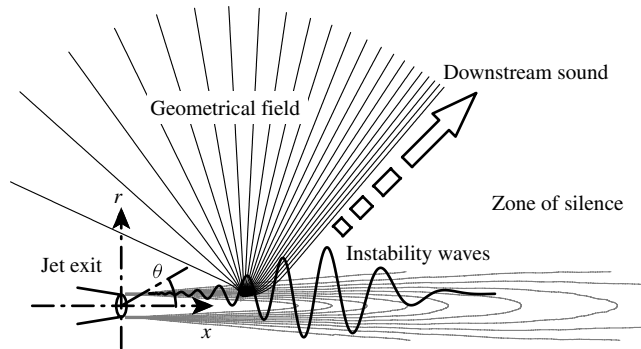
FIGURE 1. Schematic of 'classical' concept for potential jet-noise sources and regions of sound propagation.

controversial; see Crighton (1975) for earlier studies and Tam *et al.* (2008), Goldstein (2011) and Jordan & Colonius (2013) for recent ones. Although the sound pressure levels (SPLs) of unheated jets at 90° approximately follow the u_{jet}^8 law (u_{jet} being the mean jet velocity) based on a quadrupole-source model (Lighthill 1952, 1954), the prediction of the SPLs in the zone of silence is still unsatisfactory (Bridges, Khavaran & Hunter 2008) compared with the rest of the area, i.e. the geometrical field, named after geometrical optics (see figure 1). Only recently, Leib & Goldstein (2011) showed improvement in spectrum prediction including the zone of silence with specific parameters for turbulence characteristics.

Because Lighthill's equation is exact, its source computed from a full simulation should be able to recover the acoustic field (i.e. a pressure field sufficiently away from the jet) in all directions over the entire range of flow conditions. However, this source representation is less informative since the source region should be sufficiently large such that not only substantial velocity fluctuation but also mean flow must vanish at the boundary and outside this region. Many previous studies on jet noise (e.g. Phillips 1960; Ffowcs Williams 1963; Lilley 1974; Howe 1975; Mani 1976; Dowling, Ffowcs Williams & Goldstein 1978; Colonius, Lele & Moin 1997; Morris & Farassat 2002; Goldstein 2003) have attempted to distinguish the source terms and the propagation operator (i.e. the refraction effect) and to explain highly directive radiation patterns of high-speed jet noise. Although these theories have suggested quadrupole-source representations, only a few experimental studies have indicated directivity reminiscent of multipoles in unforced jets (Suzuki 2006; Lee & Bolton 2007), and their conditions were limited to low Mach numbers at low frequencies.

On the other hand, Tam, Golebiowski & Seiner (1996) viewed the jet noise as the composition of two independent source mechanisms: one associated with wavy coherent disturbances and the other originating from fine-scale turbulence. The first mechanism radiates sound downstream, while the second one is responsible for sound in the geometrical field. In essence, they attributed the highly directive sound downstream to large-scale structures in the shear layer rather than the result of refraction. Later, Tam & Auriault (1999) extended their model to fit frequency spectra with experimental data including subsonic jets. Tam and his colleagues have claimed the validity of this interpretation based on consistency with many experimental results (e.g. Laufer, Schlinker & Kaplan 1976; Viswanathan 2004; Tam *et al.* 2008). The relation between coherent structures and downstream sound has become certain as

described below; however, the independence of the two sound-generation mechanisms seems less convincing since these supporting data were acquired with simultaneous measurement of only a few microphones, if not with single microphones.

In fact, several theoretical studies (Ffowcs Williams & Kempton 1978; Tam & Morris 1980; Mankbadi & Liu 1984; Crighton & Huerre 1990; Goldstein & Leib 2005) have proposed sound-generation mechanisms associated with large-scale coherent structures over the years. The streamwise evolution of instability waves (i.e. growth, saturation and decay), forming a 'wave-packet', due to a spreading shear layer creates a small fraction of the fluctuating components with supersonic phase velocity, even for subsonically convecting jets. In particular, these fluctuations have a greater impact primarily in downstream directions. An experimental study (Ahuja 1973) reported that the peak frequency in the zone of silence is scaled differently from the geometrical field, namely the Helmholtz scaling in the zone of silence as opposed to the Strouhal scaling in the rest, and a theoretical explanation was also given (see Goldstein & Leib 2005).

Although many experimental studies (Crow & Champagne 1971; Michalke & Fuchs 1975; Maestrello & Fung 1979; Armstrong 1981; Arndt, Long & Glauser 1997; Citriniti & George 2000; Ukeiley & Ponton 2004) have observed large-scale structures associated with a round-jet shear layer in the past, it was non-trivial to compare measured quantities with the instability theories for unforced turbulent jets. Recent diagnostic tools have enabled us to probe such flow structures non-invasively; see Jordan & Gervais (2008) and Suzuki (2010). Using a phased-microphone array, Suzuki & Colonius (2006) demonstrated that pressure fluctuations just outside the upstream shear layer agree with eigenfunctions of the convective wave equation based on linear stability analysis. Reba, Simonich & Schlinker (2008) were able to recover an acoustic field of a high-Mach-number jet at a low frequency by simulating pressure fluctuations in the hydrodynamic region with a Gaussian wave-packet model and taking its statistical data from a rotating near-field microphone array. Tinney, Ukeiley & Glauser (2008) also attempted to recover sound pressure in the far field from proper-orthogonal-decomposition (POD) modes of dominant near-field velocity components. Their result captured dominant downstream sound but substantially under-estimated the SPL. Recent studies (Hileman *et al.* 2005; Suponitsky, Sandham & Morfey 2010; Cavalieri *et al.* 2011) have mentioned the importance of intermittency for effective radiation from coherent structures. These results support the sound-generation mechanism owing to coherent fluctuations associated with instability waves.

In contrast to the progress in research on the downstream-sound component, the understanding of the sound-generation mechanism responsible for the geometrical field is still limited. In particular, it is unclear if this mechanism is independent of the downstream-sound generation and if the quadrupole representation is suitable for it. Recent diagnostic tools can be used to explore these problems; however, the interpretation of such studies (e.g. Venkatesh, Polak & Narayanan 2003; Lee & Bridges 2005; Suzuki 2006; Lee & Bolton 2007; Faranosov & Kopiev 2009; Dougherty 2012) may not be straightforward because of the limited understanding of the source model itself and coherence/incoherence between the noise components. Thus, we would like to adopt a source-detection algorithm that can capture highly directive radiation patterns and identify source properties regardless of the coherency with minimal assumptions on the source model.

The objective of this study is to evaluate these source models for subsonic jets based on the phased-array data previously taken at NASA Glenn Research Center. From a near-field array, called the *hydrodynamic array* (Suzuki & Colonius 2006), we quantify

the amplitude of instability waves and reproduce an acoustic field associated with them. This study specifically takes an approach analogous to the boundary-value problem solved by Crighton & Huerre (1990) and examines three types of boundary conditions. The first one is an eigenfunction in linear stability analysis, the second one is a Gaussian wave-packet model similar to Reba *et al.* (2005), and the third one is a POD mode in a cross-spectral matrix of the hydrodynamic array. Comparison of the projected acoustic fields from these three conditions with the measured SPL at a mid-field acoustic array reveals the key features of downstream-sound generation. For the acoustic-array data originally investigated by Lee & Bridges (2005), L_1 generalized-inverse beam-forming (Suzuki 2011) is applied to investigation of both downstream and geometrical-field components. With this algorithm: (i) coherent sources can be individually detected with high resolution; (ii) the source distributions can be decomposed into any prescribed source types; and (iii) the phase relations of these sources can be identified. The capability of this algorithm was demonstrated based on a set of benchmark problems and a scale-model test in Suzuki (2011). The first two POD modes in the cross-spectral matrix of the acoustic array are processed using spherical multipoles as the reference solutions, and the source distribution and phase evolution are detected along the jet axis. In particular, the distinction between the two noise components is emphasized, and the effect of refraction is discussed.

The rest of the paper is structured as follows. After the experimental database is briefly reviewed in the next section, the projection of the hydrodynamic signals via a boundary-value problem is explained. Next, the generalized-inverse beam-forming algorithm is summarized and applied to detection of model sources in order to provide the interpretation of the source maps; subsequently, the impact of refraction is evaluated by comparing source maps composed of the free-space multipoles with those of the high-frequency asymptotic Green's functions. The results of the boundary-value problem and the beam-forming approach are then analysed at relatively low Strouhal numbers ($0.2 \lesssim St \equiv fD/u_{jet} \lesssim 0.6$, f and D being the frequency and the nozzle diameter, respectively) over a range of the Mach numbers ($0.35 \leqslant M_\infty \equiv u_{jet}/a_\infty \leqslant 0.9$, a_∞ being the ambient speed of sound). Finally, conclusions and implications are presented, referring to a series of previous studies.

2. Experimental database

The experimental databases which are post-processed in this study were acquired at NASA Glenn Research Center using the small hot jet acoustic rig (SHJAR). Details of the facility and the experimental conditions have been described in the following articles: Bridges & Wernet (2003), Bridges & Brown (2005), Lee & Bridges (2005) and Suzuki (2006) for the test using the acoustic array as well as the particle image velocimetry (PIV), and Suzuki & Colonius (2006) for the test using the hydrodynamic array. Their summaries are stated below.

2.1. *Test facility and experimental conditions*

A single-stream round jet was mounted in an anechoic dome with a 20 m radius. The exit diameter of a convergent nozzle was $D = 5.08$ cm (2.0 in). Among the Mach numbers and temperature ratios tested following Tanna's test matrix (Tanna 1977), the set points (SP) listed in table 1 are post-processed in this study. Test uncertainties and repeatability of the facility were extensively discussed by Bridges & Brown (2005).

To compute eigenfunctions in linear stability analysis and ray trajectories for source detection, mean-flow data measured by Bridges & Wernet (2003) are used. Velocity
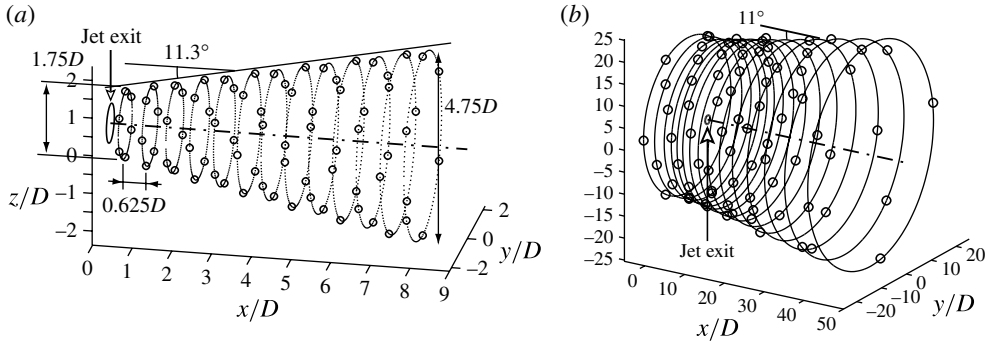
FIGURE 2. Microphone distributions of the two arrays. (*a*) Near-field hydrodynamic array (figure taken from Suzuki & Colonius 2006). (*b*) Mid-field acoustic array (figure taken from Suzuki 2006).

Set point	M_∞ (M_{jet})	T_{jet}/T_∞	Re	PIV data availability
1	0.35 (0.35)	0.98	4×10^5	No (from SP3)
3	0.50 (0.51)	0.96	7×10^5	Yes
5	0.70 (0.74)	0.91	11×10^5	No (from average of SP3 + SP7)
7	0.90 (0.98)	0.84	16×10^5	Yes

TABLE 1. List of experimental conditions. $M_\infty \equiv u_{jet}/a_\infty$, $M_{jet} \equiv (u/a)_{jet}$ and $Re \equiv (uD)_{jet}/\nu_\infty$, where the subscript ∞ denotes the ambient quantity.

fields on the axial and cross-sectional planes were measured with PIV, and frames were averaged to acquire the mean flow. Although PIV velocity fields for a few set points were not acquired, these cases are estimated by scaling the velocity from neighbouring set points ignoring compressibility, as noted in table 1.

2.2. *Microphone arrays and data processing*

Two sets of phased-microphone arrays were deployed to measure near-field pressure fluctuations and mid-field acoustic pressure waves, respectively. But, they were set in separate runs, and the measurements were separately performed. The near-field microphone array is composed of 13 rings in the axial direction with circumferentially six microphones each, a total of 78 quarter-inch microphones (see figure 2*a* for the coordinate system and the microphone positions). The axial extent from the nozzle exit to $x/D \approx 8$ is covered, and the radial positions of the microphones are placed in $0.9 \leqslant r/D \leqslant 2.4$ from the jet axis in a conical shape with the spreading angle of 11.3°. In figure 3, the baseline 'ring' positions are plotted together with one exception for SP7, the reason being explained later. The microphone distribution is designed so that the instability-wave component of pressure fluctuations (i.e. evanescent waves) can be predominantly extracted. The errors of the microphone positions were less than $0.05D$, and the aliasing error was estimated within 1.2 dB for $m = 2$, which is the highest azimuthal mode of interest; see Suzuki & Colonius (2006) for details. In phased-array processing, data from all the microphones are used simultaneously; hence, the effective azimuthal microphone count is as many as six times a few rings, and the aliasing error can be suppressed.
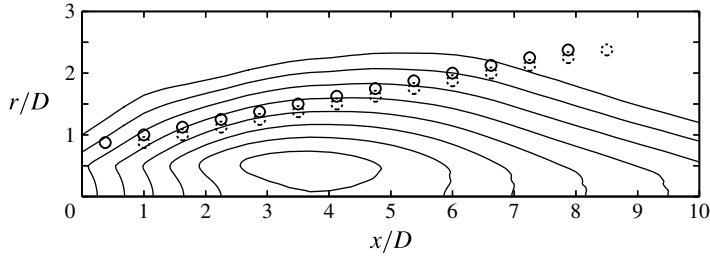

FIGURE 3. Example of an eigenfunction computed using the PIV mean-flow data for SP5 (unheated, $M_\infty = 0.7$). Pressure contours of $m = 0$ at $St = 0.35$ are drawn. Contour level -45 dB from the maximum level with 6 dB increments. Baseline microphone positions (13 rings) of the hydrodynamic array are plotted by solid ∘ (dotted ones only for SP7).

The mid-field acoustic array comprises 15 rings in the axial direction, where the upstream 10 rings have six microphones, and the downstream 5 rings have four microphones, a total of 80 quarter-inch microphones. All rings have equal circumferential spacings between the microphones, but they are in completely staggered positions between the rings. The conical array spreads nearly 11° and covers approximately $32° < \theta < 106°$ in the zenithal angles ($\theta = 0°$ pointing toward the downstream axis), where the adjacent rings are spaced roughly with an equal zenithal-angle interval, as shown in figure 2(*b*). The distances from the nozzle exit to the microphones are ranged from $17.3D$ to $48.3D$ so that purely acoustic signals are measured. The errors of the microphone positions were estimated to be less than $0.1D$ (Suzuki 2006). The aliasing error is expected to be comparable to that in the hydrodynamic array (less than 1.2 dB) as the same number of microphones are used for each ring, except the five downstream rings. Hence, the $m = 2$ modes detected from the acoustic array are not the focus of this study.

For both arrays, pressure time-histories were recorded at the sampling rate of 50 kHz and low-pass filtered at 20 kHz. They are segmented into four periods of the specified frequency with 50 % overlap to apply the discrete Fourier transforms. Because the retarded time is largely varied in the acoustic array depending on the ring positions, Fourier-transformed segments are shifted based on the retarded time assuming the source position to be at $(x/D, r/D) = (5, 0)$. Such a treatment is not made for the hydrodynamic array assuming that instability waves are formed simultaneously across the array length. Cross-spectral matrices are then generated by averaging 5000 segments. The Hann window is applied, and the corresponding power correction is made such that the broadband level (i.e. white-noise power) can be retained for both array data. Thus, the SPL projected from the hydrodynamic array can be directly compared to that in the acoustic array.

3. Projection of sound from the near-field hydrodynamic array

To examine whether pressure fluctuations given by eigenfunctions in linear stability analysis or those along the hydrodynamic array can reproduce jet noise at low frequencies, we solve a boundary-value problem analogous to Tam & Morris (1980) or Crighton & Huerre (1990). This section first reviews the procedure by Suzuki & Colonius (2006) to construct eigenfunctions representing instability waves. We also consider two additional approaches that extract pressure signals from the hydrodynamic array. The subsequent part describes the projection method equivalent

to Kirchhoff's surface-integral approach in the frequency domain. In particular, we simplify the approach by Reba *et al.* (2005) to readily compare different types of pressure fluctuations.

3.1. *Three candidates of the boundary conditions*

For the first candidate of the boundary values, eigenfunctions of a spatial problem are constructed under the assumption that the mean flow is transversely sheared and locally parallel. The mean-streamwise-velocity profiles are given from the PIV data (Bridges & Wernet 2003; Lee & Bridges 2005), and the mean-temperature profiles are estimated using the Crocco–Busemann relation (Schlichting 1960). After fitting the mean-velocity and temperature profiles with hyperbolic-tangent functions, a complex wavenumber, k_x, and the corresponding eigenfunction are calculated at each axial station, x, for each azimuthal-mode number, m; namely, the logarithmic pressure is expressed as $\hat{\Pi}(k_x, r, m)$, noted later in (3.5). Even beyond the neutrally stable point (i.e. $\text{Im}[k_x] = 0$), complex wavenumbers can be computed using the shooting method by Boyd (1985). The solutions along x are then integrated as

$$\Pi(m; x, r, \phi) = \hat{\Pi}(k_x(x), r, m) \exp\left[i\left(\int_0^x k_x(x')\,\mathrm{d}x' + m\phi\right)\right], \qquad (3.1)$$

where ϕ denotes the azimuthal coordinate. Thus, dependent variables are Fourier-transformed in time, and no symbol is used for the reminder of quantities in the frequency domain throughout this paper. They may also be azimuthally decomposed and Fourier-transformed in the axial direction in one way or another, and this is denoted by a top-hat symbol as expressed above.

Figure 3 draws the magnitude of an eigenfunction for the baseline case (SP5 for $m = 0$ at $St = 0.35$ is taken throughout this paper). As the mean-velocity profile spreads downstream, the growth rate decreases, vanishes and eventually becomes negative; accordingly, instability waves grow, saturate and decay, forming a wave-packet structure (Crighton & Huerre 1990). Unlike other candidates of the boundary conditions below, we can specify pressure fluctuations along a constant radius without extrapolation since the eigenfunctions span the x–r plane.

Coefficients of the eigenfunctions are calculated using pressure signals from the hydrodynamic array. With the normalized eigenfunction, (3.1), and the corresponding measured pressure in the frequency domain, $q_j \equiv q(x_j, r_j, \phi_j)$ appearing as its complex conjugate q_j^* below, a complex coefficient for each time segment is determined based on least-squares minimization as

$$|\hat{a}(m)|^2$$

$$= \left| \frac{\sum_{j=1}^{N_{mic}} \hat{\Pi}(k_x, r_j, m) \exp\left(-\text{Im}\left[\int_0^{x_j} k_x\,\mathrm{d}x'\right]\right) \exp\left(i\,\text{Re}\left[\int_0^{x_j} k_x\,\mathrm{d}x'\right] + im\phi_j\right) q_j^*}{\gamma \sum_{j=1}^{N_{mic}} |\hat{\Pi}(k_x, r_j, m)|^2 \exp\left(-2\,\text{Im}\left[\int_0^{x_j} k_x\,\mathrm{d}x'\right]\right)} \right|^2$$

$$(3.2)$$

(see Suzuki & Colonius 2006 for the derivation), where γ denotes the specific heat ratio and the subscript j expresses a quantity at the jth microphone. All $N_{mic} = 78$ microphones are used as opposed to only 42 upstream microphones in Suzuki & Colonius (2006) to fit the envelope of instability waves even beyond the end of the potential core (though the difference in the estimated instability-wave amplitude is

less than 1 dB, even in SP7 at $St = 0.35$). The coefficient is defined as the root mean square of (3.2), $(\overline{|\hat{a}(m)|^2})^{1/2}$, which can actually be calculated using a cross-spectral matrix of the hydrodynamic array. This algorithm is analogous to conventional beam-forming, where an eigenfunction representing instability waves is adopted as the reference solution as opposed to a point source for beam-forming.

For the rest of the two candidates of the boundary values, pressure signals are extracted from the hydrodynamic data without invoking a model based on flow physics. In the second boundary condition, the method by Reba *et al.* (2005) is modified to closely approximate measured pressure fluctuations and to impose them along a constant radius. At each ring of the array, the azimuthally decomposed pressure level at the lth ($1 \leqslant l \leqslant 13$) axial station, $\hat{q}_l(m) \equiv \hat{q}(m; x_l, r_l)$, is calculated. Subsequently, the phase part is progressively determined from two adjacent rings in the axial direction:

$$\left.\begin{array}{ll} \overline{|\hat{q}_l(m)|} & \text{for } l = 1, \\[2mm] \overline{|\hat{q}_l(m)|} \exp\left[i \sum_{l'=2}^{l} \arg(\overline{\hat{q}_{l'-1}^*(m)\hat{q}_{l'}(m)})\right] & \text{for } l \geqslant 2, \end{array}\right\} \qquad (3.3)$$

where $l = 1$ is taken as the reference station for the phase. In essence, pressure fluctuations are averaged by taking the information from the tri-diagonal part of the cross-spectral matrix.

For the third candidate of the boundary values, the first POD mode is extracted from a cross-spectral matrix of the hydrodynamic array. A column vector $\boldsymbol{q}$ is now composed of azimuthally decomposed pressures, $\hat{q}_l(m)$, across all the axial stations; hence, a 13×13 cross-spectral matrix can be generated for each m. Because it is Hermitian and positive definite, we can decompose it as

$$\overline{\boldsymbol{q}\boldsymbol{q}^\dagger} = \boldsymbol{U}\boldsymbol{\Lambda}\boldsymbol{U}^{-1}, \qquad (3.4)$$

where $\boldsymbol{\Lambda}$ denotes a diagonal matrix comprising positive eigenvalues, and $\boldsymbol{U}$ consists of their orthonormal eigenvectors (i.e. a set of unit orthogonal vectors). Using an eigenvalue and the corresponding orthonormal eigenvector, we define the first POD mode to be $\sqrt{\lambda_1}\boldsymbol{u}_1$. This mode specifically represents a coherent structure occupying the largest 'energy' of the cross-spectral matrix.

These three boundary conditions representing a wave-packet along the hydrodynamic array are compared in figure 4. The evolution of the magnitude of the second boundary condition, (3.3), is approximated by the formula, $\alpha x^{\mu-1} \exp(-\mu x/x_0)$ (α, μ and x_0 are parameters to be determined; see Tester & Glegg 2008). In contrast, that of the first POD mode is fitted with a Gaussian shape since the envelopes of the POD modes are damped more rapidly than those of the second boundary condition. Away from the most unstable frequency, it is difficult to fit the measured envelopes with these analytic functions, and this restricts the frequency range of this study ($0.25 \leqslant St \leqslant 0.50$) using the hydrodynamic array. In figure 4(*a*), all of them depict the evolution of shear-layer disturbances, i.e. growth, saturation and decay. Although their peak levels are similar, the decay rates downstream differ noticeably.

The phase evolutions are similarly compared in figure 4(*b*), where values of the second and third boundary conditions are fitted with third-order polynomials. Their slopes correspond to the local wavenumber. The wavenumber of the eigenfunction from linear stability analysis, which assumes the mean flow to be locally parallel, is clearly higher than the other two boundary conditions toward downstream, leading to slower phase velocity. Gudmundsson & Colonius (2011) calculated eigenfunctions
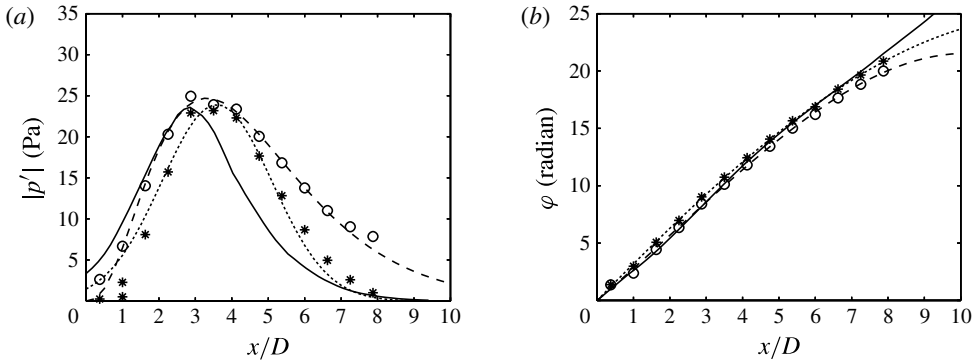
FIGURE 4. Comparison of the three boundary conditions along the hydrodynamic array (spreading at $11°$). Conditions are the same as figure 3. (*a*) Magnitude of pressure fluctuations. (*b*) Phase evolution of pressure fluctuations. Notation: ——, eigenfunction; $-\circ-$, averaged fluctuations (second candidate); $\cdots*\cdots$, first POD mode (third candidate).
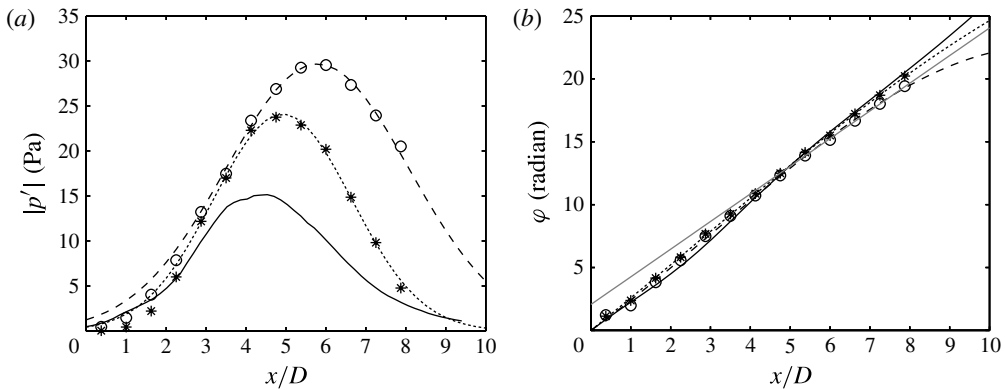
FIGURE 5. Comparison of the three boundary conditions at a constant radius ($r_0/D = 1.625$). Conditions and notation are the same as figure 4. (*a*) Magnitude of pressure fluctuations. (*b*) Phase evolution of pressure fluctuations. The phase velocity corresponding to u_{jet} is also drawn with a straight grey line for reference.

using the same PIV data with the linear parabolized stability equation. Their comparison with these two boundary conditions still show similar trends downstream, suggesting that the effect of shear-layer spreading cannot by itself explain the discrepancy between the eigenfunctions and the measured data.

These three candidates of the boundary condition are now plotted at a constant radius ($r_0/D = 1.625$, the centre of the array) in figure 5. With the local wavenumbers computed from figure 4(*b*), we can derive the radial decay rates, which are given by the Hankel function in (3.5) later; accordingly, complex values are transferred from the array positions to the constant radius for the second and third boundary conditions. Their magnitude envelopes are well represented by the Gaussian profiles, even for the second condition, and the phase evolutions are similarly fitted with third-order polynomials. These analytic profiles are iteratively calculated. It is noted that the radial position actually chosen later for projection of the first boundary condition, (i.e. eigenfunction) is closer than $r_0/D = 1.625$.

Figure 5(*a*) shows that the three profiles now become completely distinguishable: the second condition representing the averaged pressure fluctuations grows to the highest peak level with the slowest decay, while the eigenfunction peaks most upstream and tends to stay with the lowest level. The discrepancies of the decay rates and the wavenumbers in figure 4 escalate along the constant radius in figure 5. The phase evolutions in figure 5(*b*) indicate that the second boundary condition provides the smallest wavenumber, i.e. the highest phase velocity, $\sim u_{jet}$ or higher, downstream. We discuss their differences in further detail in §5.1.

3.2. *Projection method via a boundary-value problem*

By imposing each of the three candidates as the near-field boundary condition, its acoustic field can be calculated respectively. At a constant radius, $r = r_0$, beyond which the mean velocity is neglected, (3.1) is Fourier-transformed in x. Because the domain where the PIV data are available is limited (see figure 3), the eigenfunctions are extended to $-1000 \lesssim x/D \lesssim 1000$, referring to the exponents of the growth and decay rates on both ends of the PIV domain. Assuming all waves are outgoing at r_0, pressure fluctuations of the mth azimuthal mode at an outer radius, r, can be obtained as

$$\frac{1}{\gamma} \frac{p'_m}{p_\infty} \approx \frac{1}{\gamma} \log \left| 1 + \frac{p'_m}{p_\infty} \right|$$

$$= \sqrt{\overline{|\hat{a}(m)|^2}} \int_{-\infty}^{\infty} \frac{\mathrm{H}_m^{(1)} \left(r\sqrt{(\omega/a_\infty)^2 - k_x^2} \right)}{\mathrm{H}_m^{(1)} \left(r_0\sqrt{(\omega/a_\infty)^2 - k_x^2} \right)} \mathscr{F}[\hat{\Pi}(m; x, r_0, \phi)] \exp[\mathrm{i}k_x x] \, \mathrm{d}k_x, \quad (3.5)$$

where $\mathrm{H}_m^{(1)}$ denotes the Hankel function of the first kind of order m, p_∞ is the ambient pressure, and $\mathscr{F}$ represents a Fourier transform operator in x as a function of k_x.

When the pressure fluctuations are extracted from the hydrodynamic array for the second and third candidates, the boundary position, r_0, is selected at the centre of the array, $r_0/D = 1.625$, to minimize the extrapolation errors. For the eigenfunctions, however, attention should be paid to the determination of r_0. If the mean flow were perfectly parallel, the eigenfunction would generate only evanescent waves in the radial direction, that is, no generation of sound in the far-field. The spreading rate of the shear layer causes the axial wavenumber to vary slowly, creating a fraction of supersonic phase-velocity components. The eigenfunctions themselves carry no acoustic waves, but their wavenumber variation mainly generates sound via the projection (an explanatory diagram can be found in Tam *et al.* 2008). Therefore, we wish to avoid excessive radial decay of the eigenfunctions by taking r_0 closer to the shear layer, but it must still be sufficiently far from the finite-Mach-number region of the mean flow to apply the Hankel function for free-space wave propagation.

Figure 6 compares the radial decay between the eigenfunction and the projected pressure signals using (3.5) for $m = 0$, indicating their overlapped region. When r_0 is too close to the shear layer, the profiles of the eigenfunction and the projected acoustic field do not smoothly connect to each other. On the other hand, the far-field pressure level keeps decreasing with increasing r_0 because the hydrodynamic field transitions into the acoustic field in a lower disturbance level at an outer radius. We revisit the dependence on r_0 in §5.1.

In Reba *et al.* (2005), the Neumann boundary condition was imposed upstream of the nozzle exit; subsequently, the Wiener–Hopf technique was used to project the
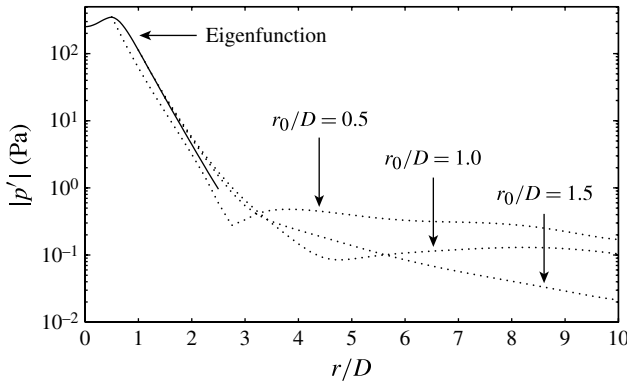
FIGURE 6. Comparison of the radial pressure profiles for different radial boundary positions r_0. Magnitudes of the pressure disturbances at $x/D = 4$ are plotted. The eigenfunction based on the linear stability analysis is drawn by ——, and the projected signals by $\cdots\cdots$. The flow conditions are the same as figure 3 (i.e. unheated, $M_\infty = 0.7$ for $St = 0.35$ and $m = 0$).

acoustic field. To be precise, however, the nozzle lip is positioned inside the extension of the microphone array conical surface (see figure 3). Even for the eigenfunctions, a suitable r_0 is also found to be outside the nozzle-lip line (i.e. $r/D = 0.5$) from figure 6. Thus, the radial positions of the boundary conditions are always outside the lip line in this study, especially because they are taken at constant radii; accordingly, the boundary conditions are infinitely extended upstream in analytical manners for all three boundary conditions.

4. Detection of source distribution from the mid-field acoustic array

4.1. *Multipoles for the reference solutions*

In the next analysis, an attempt is made to represent the noise source as collection of multipoles. The idea behind it is not necessarily motivated by the quadrupole-source theory for aerodynamic sound (Lighthill 1952). Since arbitrary far-field directivity from a compact source can be expanded by a series of multipoles (Oestreicher 1957), the hope is that the jet-noise source can be approximated by a distribution consisting of a limited number of lower-order multipoles. Once their distribution/combination including the phase relation can be appropriately identified among non-unique solutions, the acoustic fields even outside the microphone array coverage should be recovered in principle, if these multipoles are solutions to the field of our interests, at least in an approximate sense.

For simplicity, the spherical multipoles in the free space are primarily used as the reference solutions. The underlying assumption is that the region associated with the sheared mean flow is considered as a part of a compact source. But, the other limit, i.e. high-frequency asymptotic solutions, will be examined later to evaluate the refraction effect. The radiation patterns of the free-space multipoles are expressed by the associated Legendre functions as

$$P_n^m(\cos\theta) \equiv \frac{(-1)^{m+n}}{2^n n!} \sin^m\theta \frac{\mathrm{d}^{m+n}}{\mathrm{d}(\cos\theta)^{m+n}} \sin^{2n}\theta, \qquad (4.1)$$

with $n \geqslant m$. To be precise, the coefficients are normalized such that the integral over the entire sphere is set to be equal for all the modes (see figure 7). Considering
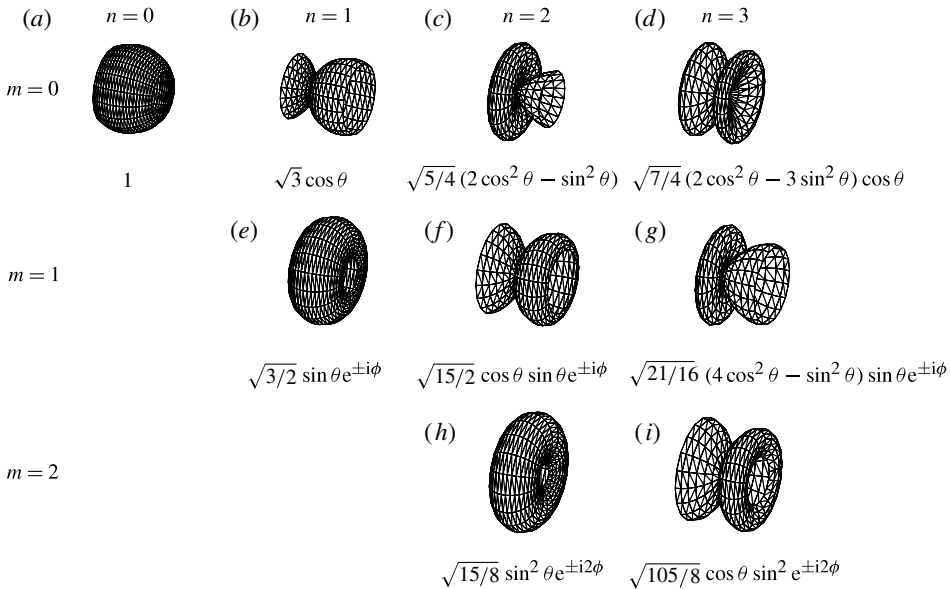
(a) $n = 0$ (b) $n = 1$ (c) $n = 2$ (d) $n = 3$

$m = 0$

1    $\sqrt{3}\cos\theta$ $\sqrt{5/4}\,(2\cos^2\theta - \sin^2\theta)$ $\sqrt{7/4}\,(2\cos^2\theta - 3\sin^2\theta)\cos\theta$

(e) (f) (g)

$m = 1$

$\sqrt{3/2}\,\sin\theta\,\mathrm{e}^{\pm\mathrm{i}\phi}$ $\sqrt{15/2}\,\cos\theta\sin\theta\,\mathrm{e}^{\pm\mathrm{i}\phi}$ $\sqrt{21/16}\,(4\cos^2\theta - \sin^2\theta)\sin\theta\,\mathrm{e}^{\pm\mathrm{i}\phi}$

(h) (i)

$m = 2$

$\sqrt{15/8}\,\sin^2\theta\,\mathrm{e}^{\pm\mathrm{i}2\phi}$ $\sqrt{105/8}\,\cos\theta\sin^2\theta\,\mathrm{e}^{\pm\mathrm{i}2\phi}$

FIGURE 7. Radiation patterns of the free-space multipoles. The jet is ejected from left to right. Only the range of zenithal angles covered by the acoustic array is drawn assuming the source position to be at $x/D = 5$.

computational cost, modes up to $n = 3$ (i.e. octupole) for each azimuthal modes (i.e. $m = 0, \pm 1$ and ± 2) are prepared. However, only the results of non-negative azimuthal modes are shown in this paper since no major differences are discerned statistically between opposite azimuthal modes.

4.2. *Source mapping with L_1 generalized-inverse beam-forming*

To map the source distribution specifically associated with the coherent signals, L_1 generalized-inverse beam-forming (Suzuki 2011) is applied to the acoustic-array data. In Suzuki (2006), the same database was analysed using robust adaptive beam-forming with the aforementioned multipoles as the reference solutions. In this previous approach, however, the orientation of multipoles must be predefined, and the directivity and SPL cannot be recovered from the detected source distributions. In contrast, the L_1 generalized-inverse algorithm is able to identify complex source-amplitude distributions of arbitrarily oriented multipoles for each coherent signal. Unlike other existing beam-forming algorithms, this algorithm minimizes ambiguities associated with the source models.

By expressing the array of measured pressure with a column vector $\boldsymbol{q}$ in the frequency domain, a cross-spectral matrix of the acoustic array is first decomposed into

$$\overline{\boldsymbol{q}\boldsymbol{q}^{\dagger}} = \boldsymbol{U}\boldsymbol{\Lambda}\boldsymbol{U}^{-1}. \tag{4.2}$$

Using an eigenvalue and its orthonormal eigenvector, we similarly define the ith POD mode as $\boldsymbol{v}_i \equiv \sqrt{\lambda_i}\boldsymbol{u}_i$ such that $\sum_{i=1}^{N_{mic}} \boldsymbol{v}_i \boldsymbol{v}_i^{\dagger}$ recovers the cross-spectral matrix.

Second, using generalized-inverse techniques, we attempt to solve the complex source-amplitude distribution, $\boldsymbol{a}_i$, which includes all the reference solutions together

across all grid points and recovers each POD mode via a transfer function, $\boldsymbol{A}$, as

$$\boldsymbol{v}_i = \boldsymbol{A}\boldsymbol{a}_i. \tag{4.3}$$

In this study, the number of microphones is fewer than the number of source types (i.e. multipoles) times the number of source points (i.e. grids); namely, $\boldsymbol{A}$ is an N_{mic} by $N_{type} \times N_{grid}$ matrix, and an under-determined problem is considered. An initial source distribution consisting of prescribed source types, $\boldsymbol{a}_i$, is then calculated for each mode i with a least-squares approach.

Finally, the following L_1 norm is minimized using iteratively reweighted least squares (IRLS) following Huber (1981):

$$J_1 \equiv \sum^{N_{type} \times N_{grid}} |a_i| + \boldsymbol{\lambda} \cdot (\boldsymbol{v}_i - \boldsymbol{A}\boldsymbol{a}_i), \tag{4.4}$$

where a_i denotes an individual component of the vector $\boldsymbol{a}_i$, and $\boldsymbol{\lambda}$ is the Lagrangian-multiplier vector. This signifies that the algorithm attempts to find a source distribution minimizing its L_1 norm with the constraint of recovering the coherent signal at the microphones. By solving an under-determined generalized-inverse problem for each POD mode of the cross-spectral matrix, we can generate a source map of each coherent signal (i.e. selected POD mode) consisting of all prescribed source types. The procedure is summarized in appendix A.

The source positions are defined over $-15 \leqslant x/D \leqslant 25$ (i.e. the target domain) with an equal spacing of $0.1D$. Consequently, the number of components for $\boldsymbol{a}_i$ counts $N_{type} \times N_{grid}$, which is, for example, $4 \times 401 = 1604$ for $m = 0$. Two POD modes are processed for each case as the first mode typically represents sound propagating downstream and the second mode sound propagating over wider angles upstream. For regularization in (A 1) and (A 2) in appendix A, the diagonal part is set to be $\epsilon = 0.01 \times$ (greatest eigenvalue of $\boldsymbol{A}\boldsymbol{A}^\dagger$ or $\boldsymbol{A}\boldsymbol{W}_i^{(n)}\boldsymbol{A}^\dagger$). The number of iterations is designated as $n = 20$, by which the L_1 norm (4.4) is mostly converged.

For reference, the eigenvalue distribution and its azimuthal-mode balance of the first six eigenvectors for SP5 at $St = 0.35$ are displayed in figure 8. Here, the square of the azimuthally decomposed pressure is summed over the zenithal angles for each POD mode. Although the distance from the source to the microphone is greater at downstream microphones, the SPL tends to be still higher downstream than upstream; hence, the downstream microphones are more weighted in effect. At a low frequency, the eigenvalues decay relatively fast with increasing mode number. Although the second and the third POD modes indicate coupling of $m = \pm 1$ and $m = \pm 3$, the other modes show a single distinctive azimuthal mode including opposite signs. In general, there are relatively few azimuthal-mode couplings over various Strouhal numbers and Mach numbers. Thus, we analyse source maps based on azimuthally decomposed cross-spectral matrices.

To understand how the generalized-inverse beam-forming algorithm identifies noise sources associated with the downstream sound, we first impose the model-source distribution corresponding to the second boundary condition in § 3.1, which is found to be the best representation in § 5.1. With the assumption for a line source, we divide the complex pressure profile in figure 5 by $(i/4)H_m^{(1)}(\omega r_0/a_\infty)$ to correct the distance and impose the same Gaussian shape with the phase profile obtained from (3.3) along the jet axis.

Figure 9 plots the detected magnitudes and phases (i.e. $|a_i|^2$ and $\arg[a_i]$) of the prescribed sources in $m = 0$ along the jet axis for the baseline condition (i.e. SP5
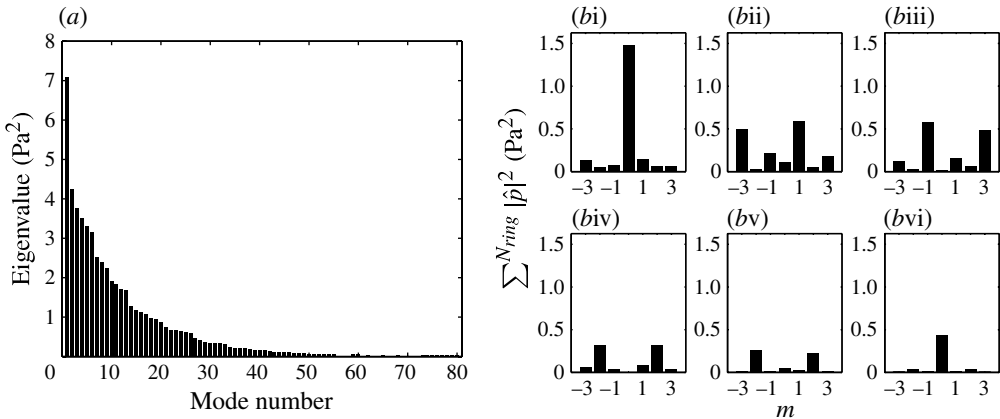
FIGURE 8. (*a*) Eigenvalue distribution of the full cross-spectral matrix for SP5 (unheated, $M_\infty = 0.7$) at $St = 0.35$. (*b*) Their azimuthal-mode balance of the first six eigenvectors. The square of the azimuthally decomposed pressure fluctuations is summed over all 15 microphone rings: (i) first mode, (ii) second mode, (iii) third mode, (iv) fourth mode, (v) fifth mode, (vi) sixth mode.
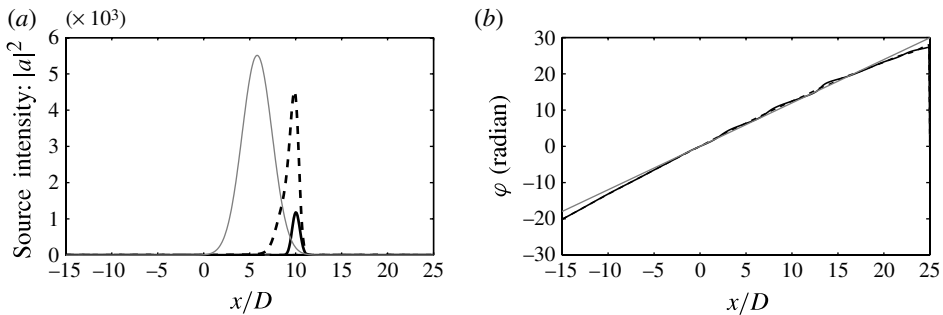

FIGURE 9. Detected source distributions of the model source corresponding to the second boundary condition in figure 5 (SP5 and $m = 0$ at $St = 0.35$). (*a*) Source maps. Line patterns: ——, $(m, n) = (0, 0)$; – – –, $(0, 1)$; – · – · –, $(0, 2)$; · · · ·, $(0, 3)$. A thin grey line denotes the original distribution $\times\, 0.1$. (*b*) Phase evolutions of the first two dominant multipoles. Line patterns are the same as (*a*). A straight grey line represents the phase velocity of $1.3a_\infty$.

at $St = 0.35$). For reference, a grey line indicates the original source profile in figure 9(*a*), but scaled down by a factor of ten. The beam-forming algorithm detects the major sources as the $(m, n) = (0, 1)$ and $(0, 0)$ modes downstream of the original distribution, but their magnitudes are a few orders smaller than the original (the magnitudes should be evaluated as integrated values, $|\int a_i\, \mathrm{d}x|$, not squared values or a peak). This is not surprising because the algorithm can detect only components with supersonic phase velocity. In fact, figure 9(*b*) captures nearly a constant phase slope of $\sim 1.3a_\infty$, which is drawn by a grey line. Although the phase velocity of the original source distribution is mostly less than u_{jet} in figure 5(*b*) except $x/D \gtrsim 10$, the wave-packet structure generates supersonic phase components, and the generalized-inverse algorithm reconstructs an equivalent source distribution that can generate sound more efficiently.
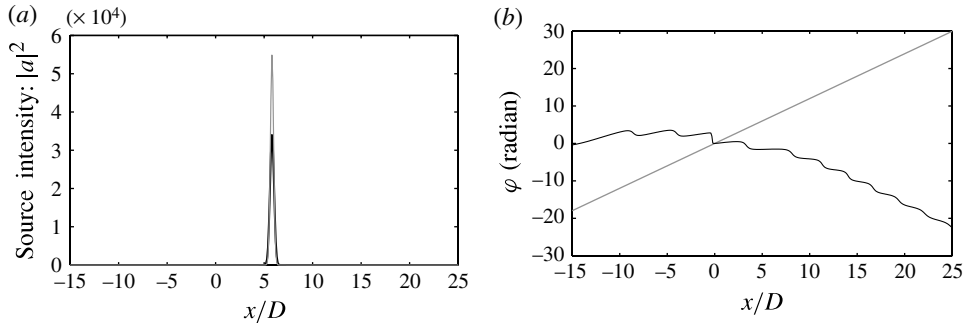
FIGURE 10. Detected source distributions of the monopole-like model source. Line patterns are the same as figure 9 unless otherwise noted. (*a*) Source maps. A thin grey line denotes the original distribution. (*b*) Phase evolution of the primary multipole.

It is important to note that the problem throughout this study is an under-determined problem, and the L_1 generalized-inverse beam-forming seeks the solution that minimizes the $|a_i|$ norm in (4.4) among those which recover the signals at the microphone positions. As a result, the algorithm tends to reconstruct a source distribution with the phase velocity higher than the original one. For unheated subsonic jets, the original phase velocity is most likely subsonic over the axial distance, leading to the detected phase velocity of approximately $\sim 1.3a_\infty$. Appendix B investigates the relation between the original and the detected phase velocities based on this model source.

Next, we attempt to map a localized source by compressing the width of the Gaussian profile by a factor of ten and imposing a constant phase; accordingly, the source nearly acts as a monopole. Figure 10 similarly displays the magnitudes and phases of the detected sources. The beam-forming algorithm can pinpoint the source position and recover the integrated source intensity within 0.05 dB relative to the original intensity. A substantial difference from the previous source is that the detected phase evolution indicates a spreading-radiation pattern. Thus, the proposed algorithm can clearly distinguish source characteristics between a wavy type and a localized type.

4.3. *Recovery of coherent signals and the refraction effect*

We now take an example of primary POD modes directly from the actual data in the baseline condition (i.e. SP5 for $m = 0$ at $St = 0.35$). At the same time, we ensure suitability of the free-space multipoles as the reference solutions. By comparing the results based on the free-space multipoles with those based on Green's functions in a jet, we crudely evaluate the effect of refraction in source mapping. In particular, we apply high-frequency Green's functions at relatively low Strouhal numbers in this section; however, the high-frequency limit is actually applicable to the frequency range in which the wavelength is even comparable to the length scale of the medium (Suzuki & Lele 2003; Wundrow & Khavaran 2004). Because the refracted angles across the shear layer are the same regardless of the frequency, we expect that the arclengths solved by the ray-tracing equations can be practically used for beam-forming over a wide range of frequency (in fact, the detected source properties are found to be similar from $St \approx 1$ down to 0.2, as discussed in §5.2).
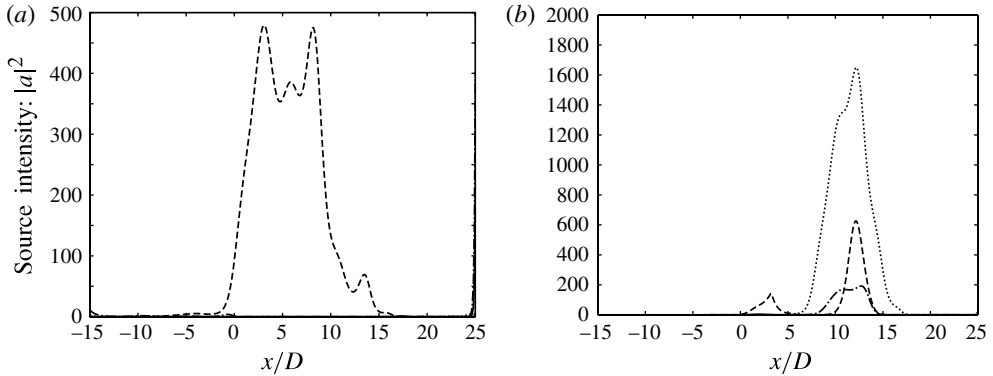
FIGURE 11. Comparison of the source maps for the first POD mode of the baseline condition, i.e. $m = 0$ at $St = 0.35$ for SP5 (unheated, $M_\infty = 0.7$). Line patterns: ——, $(m, n) = (0, 0)$; − − −, $(0, 1)$; − · − · −, $(0, 2)$; · · · · ·, $(0, 3)$. (*a*) Using free-space multipoles. (*b*) Asymptotic Green's functions.

An approach introducing asymptotic Green's functions is similar to the analysis of some previous studies (Tester & Morfey 1976; Wundrow & Khavaran 2004; Faranosov & Kopiev 2009); namely, the mean flow is assumed to be transversely sheared and locally parallel. However, unlike those studies, the distances from the sources to the microphones are not far enough to apply the stationary-phase method. In particular, ray trajectories become nearly parallel in the zone of silence (see rays downstream in figure 31 of § C.2), called refracted arrival waves (Howe 1970; Suzuki & Lele 2002), and the turning-point analysis is impractical for such waves. In turn, it is rather convenient to first construct the multipole solutions in the vicinity of the source, and then the propagation part is solved by taking the idea from Goldstein (1982) or Durbin (1983). Subsequently, asymptotic multipole factors in a jet are multiplied by the monopole solution whose directivity is computed based on the ray-tracing equations using PIV mean flow (Bridges & Wernet 2003; Lee & Bridges 2005). Details of the procedure are described in appendix C.

Figure 11 compares the source distributions for the first POD mode composed of the free-space multipoles with those of the asymptotic Green's functions. Here, we express the source intensity such that $|p'|^2 = |\int \boldsymbol{Aa}_i \, \mathrm{d}x|^2$ recovers the SPL (the distances, such as x and r, are normalized by D). While the dominant source appears in $0 \lesssim x/D \lesssim 15$ with the free-space multipoles, the sources consisting of the high-frequency multipoles shift downstream. The radiation pattern is identified as $(m, n) = (0, 1)$ for the former one and changed to primarily $(0, 3)$ for the latter due to refraction. In figure 11(*a*), an appreciable intensity of $(m, n) = (0, 2)$ is found with a high peak at $x/D = 25$, which is discussed below.

More importantly, the agreement between the first POD mode and the complex pressure recovered from the source distribution (i.e. $\boldsymbol{v}_1$ and $\boldsymbol{Aa}_1$ in (4.3), respectively) is much better using the free-space multipoles than the asymptotic Green's functions in figure 12(*a*). This strongly supports the suitability of the free-space multipoles as the reference solutions. In fact, their source distributions are able to recover the first POD mode relatively well in figure 12(*b*), while the linear combination of the asymptotic Green's functions misses the peak SPL significantly. Here, contributions of the sources only within $-5 \leqslant x/D \leqslant 20$ are integrated to avoid spurious sources mentioned above.
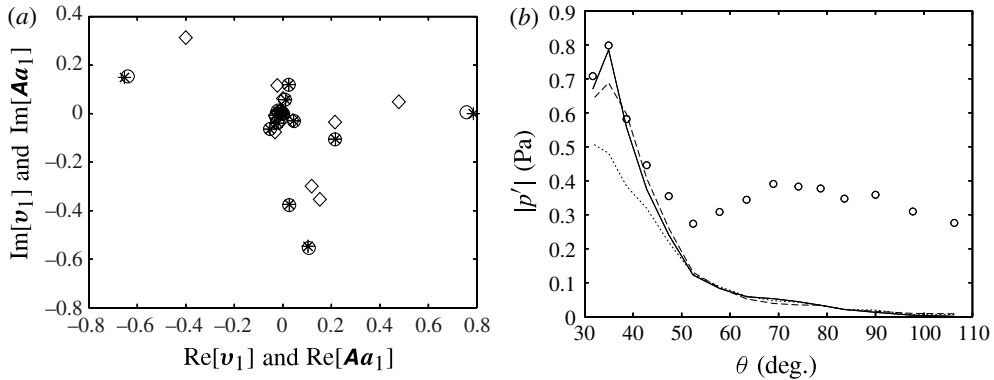
FIGURE 12. Comparison of the recovered pressure between the two sets of the reference solutions. Conditions are the same as figure 11. (*a*) Comparison on the complex plane between the first POD mode (i.e. v_1) and the corresponding Fourier-transformed pressure recovered from the source distribution (i.e. Aa_1). Symbols: ∗, first POD mode to be recovered; ○, recovered complex pressure with the free-space multipoles; ◇, that with the asymptotic Green's functions. (*b*) Recovered SPL at the microphone positions. Symbols: ○, SPL of measured auto-correlation. Line patterns: ——, first POD mode to be recovered; − − −, recovered SPL with the free-space multipoles; · · · · ·, that with the asymptotic Green's functions.

In the same test at a higher frequency (i.e. $St = 0.6$), the recovery based on the asymptotic Green's functions deteriorates further: major source distributions for the first POD mode cannot be found within a suitable range along the jet axis (not shown). Over the ranges of the Strouhal numbers and the Mach numbers studied here, better agreement is always obtained using the free-space multipoles for modes representing the downstream sound.

On the other hand, the source distributions for the second POD mode shown in figure 13(*a*) create no spurious sources at the edges of the domain: even using the asymptotic Green's functions, the distributions are localized within $0 \lesssim x/D \lesssim 10$ (those using the free-space multipoles are plotted in figure 21*a*ii in §5.2). The radiation pattern spreading over wider zenithal angles is recovered equally well by both sets of the reference solutions (almost overlapped) in figure 13(*b*). This can be understood from figure 31 in §C.2, in which rays in the geometrical field are spread almost spherically.

These results suggest that a set of the free-space multipoles can better reconstruct the coherent sound propagating downstream. The major differences between the two sets of the reference solutions are their amplitude and phase downstream. The radiation pattern becomes highly directive at higher Mach numbers; however, the actual peak angle tends to be lower than the peak of the refracted Green's functions, and they cannot capture the signal downstream well. Although the asymptotic solutions represent extreme cases, namely high-frequency sources localized along the jet axis, it is fair to assert that the highly directive sound radiation downstream is not primarily caused by refraction (in this sense, the classical definition of the 'zone of silence' may not be appropriate to express the low SPL region downstream). In the acoustic field upstream, on the other hand, both sets recover the second POD mode equally well, and the results of source mapping seem to be less sensitive to the choice of reference solutions. Thus, all beam-forming results are processed using the free-space multipoles in §5.2.
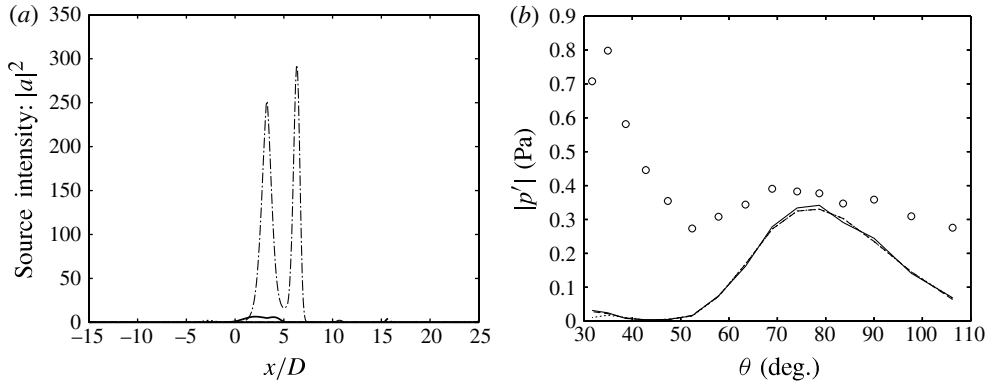
FIGURE 13. Results of beam-forming for the second POD mode of the baseline condition (i.e. $m = 0$ at $St = 0.35$ for SP5). (*a*) Source maps using the asymptotic Green's functions. Line patterns are the same as figure 11. (*b*) Recovered SPL at the microphone positions. Line patterns and symbols are the same as figure 12(*b*).

It is noticeable that some spurious sources are found at the edges of the target domain. In the example above, a sharp peak of $(m, n) = (0, 2)$ is formed at $x/D = 25$ in figure 11(*a*). Sources of this type are created more frequently using the asymptotic Green's functions rather than the free-space multipoles. Even if the domain is extended downstream, these peaks are still found at the end of the domain. They are merely created to satisfy the constraint term in (4.4), typically when unidentifiable/unresolvable signals for the prescribed solutions are contaminated. With peculiar source distributions extending to unrealistic locations, the contaminated signals may be somehow imitated. This artifact can be alleviated by increasing the number of reference solutions. By introducing octupoles, a greater variety of radiation patterns can be recovered, although they may not be physically appropriate representations (i.e. only as equivalent sources).

5. Results and discussion

5.1. *Acoustic fields projected from hydrodynamic pressure fluctuations*

We begin by observing the projected acoustic fields for the baseline case (SP5 of $m = 0$ at $St = 0.35$) solved as a boundary-value problem. Figure 14 compares instantaneous pressure fields generated from the three different boundary conditions explained in § 3.1. All of them depict a wave-packet structure in the near field and form a strong peak of sound radiation at downstream angles. Such transition from hydrodynamic to acoustic fields is qualitatively consistent with the analytical wave-packet model by Crighton & Huerre (1990). The solution from the eigenfunction in figure 14(*a*) shows a secondary peak near 90°, resulting in phase discontinuity of the acoustic field. Importantly, the second expression in figure 14(*b*) produces the amplitude an order of magnitude higher than the other two boundary conditions.

Next, we compare these projected SPLs with those measured at the mid-field acoustic array. For the measured quantities, we generate an azimuthally decomposed cross-spectral matrix from the acoustic array and extract the first and second POD modes as well as the diagonal part representing the auto-correlation. Symbols in figure 15 indicate that the first POD mode captures a coherent component propagating downstream, while the second mode represents a component radiating more widely
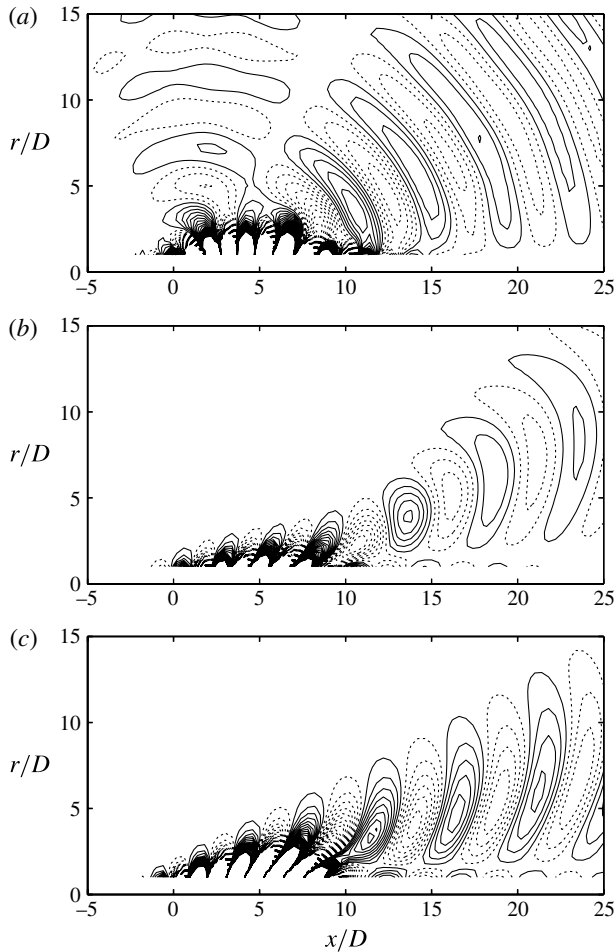
FIGURE 14. Comparison of the projected pressure fields solved via the boundary-value problem (SP5 of $m = 0$ at $St = 0.35$). Real parts of (3.5) for the three boundary conditions are drawn. Solid and dotted lines denote opposite signs of pressure fluctuations. (*a*) Solution from the eigenfunction ($r_0/D = 1.0$). Contour levels -2.45 Pa $\leqslant \text{Re}[p'] \leqslant 2.45$ Pa with 0.1 Pa increment. (*b*) Averaged pressure fluctuations from the hydrodynamic array ($r_0/D = 1.625$). Contour levels -24.5 Pa $\leqslant \text{Re}[p'] \leqslant 24.5$ Pa with 1.0 Pa increment. (*c*) First POD mode from the hydrodynamic array ($r_0/D = 1.625$). Contour levels are the same as (*a*).

over $60° \lesssim \theta \lesssim 100°$. In general, the first two POD modes respectively exhibit similar trends in other conditions as well. The shift of the retarded time in generating the cross-spectral matrix helps extract two distinctive modes. Here, we should recall that the distances from the nozzle to downstream microphones are farther than those to upstream ones; hence, the following plots tend to de-emphasize the directivity of the downstream sound.

Figure 15(*a*) additionally compares these measured quantities with the SPLs generated based on the eigenfunction at three different radial positions of the boundary condition. Although the projected SPL increases by shifting r_0 closer to the jet axis, the $r_0/D = 0.5$ case still under-predicts the auto-correlation level as much as 15 dB over the entire angles. Namely, even if we take r_0 near the peak of the eigenfunction
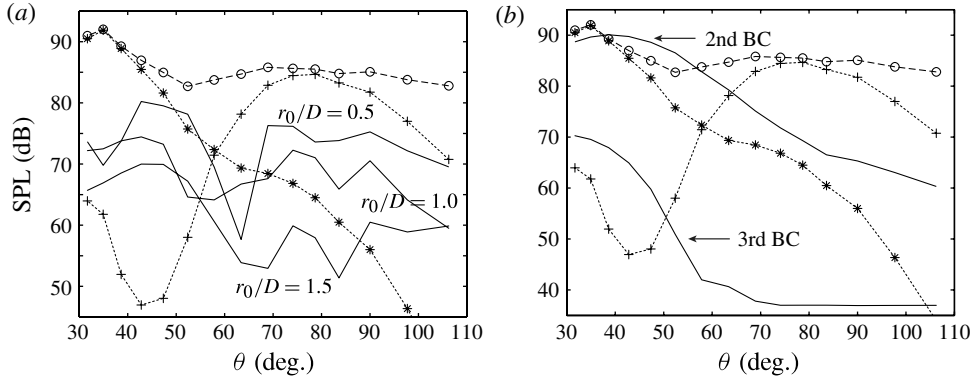
FIGURE 15. Comparison of the SPLs for the axisymmetric mode at the mid-field acoustic-array positions. Conditions are the same as figure 14 ($M_\infty = 0.7$, $St = 0.35$ and $m = 0$). Zenithal angles are measured from the nozzle exit. Symbols are calculated from the cross-spectral matrix of the acoustic array (common to both figures): $-\circ-$, diagonal (auto-correlation); $\cdots*\cdots$, first POD mode; $\cdots+\cdots$, second POD mode. (*a*) Projection of the eigenfunction (drawn by three solid lines). (*b*) Projection of the signals from the hydrodynamic array (two boundary conditions drawn by solid lines).

(see figure 6), in which the mean flow is no longer quiescent, the projected SPL is still too low. Moreover, the recovered directivity captures neither first nor second POD modes at the acoustic array.

In contrast, figure 15(*b*) shows that the projection from the averaged pressure fluctuation at the hydrodynamic array (i.e. the second boundary condition) approximately recovers the SPL downstream and decays upstream. Such directivity is similar to the first POD mode from the acoustic array. The projection of the first POD mode from the hydrodynamic array (i.e. the third condition) still vastly under-estimates the SPL. We have observed in figures 4 and 5 that the major differences between these two boundary conditions are the streamwise decay and the phase velocity beyond the end of the potential core. In fact, the second condition has the greatest magnitude and the fastest phase velocity in figure 5. For the rest of the discussion, only the projections from the first boundary condition at $r_0/D = 1$ (the closest radius among the profiles with smooth transition in figure 6) and from the second condition are compared with the measured SPL at the acoustic array.

We find similar features in the projections of azimuthal modes. Figure 16 again demonstrates that the second boundary condition captures the downstream SPL much better than the other conditions (the third boundary condition also far under-predicts the SPL, not shown). To be precise, the measured auto-correlation for $m = 2$ is somewhat higher than both POD modes and projection of the second boundary condition in figure 16(*b*); however, the downstream five rings of the mid-field acoustic array can contain more aliasing errors than other rings because they consist of only four microphones as opposed to six. In contrast, all the rings in the hydrodynamic array have six microphones. Likewise, even the POD modes of the acoustic array may possibly suppress aliasing errors from higher azimuthal modes as they extract coherent signals across all the rings. Thus, the under-prediction for $m = 2$ is understandable in $\theta < 50°$.

Even at lower and higher Mach numbers in figures 17 and 18, respectively, the trend remains the same: the first POD mode of the acoustic array captures the
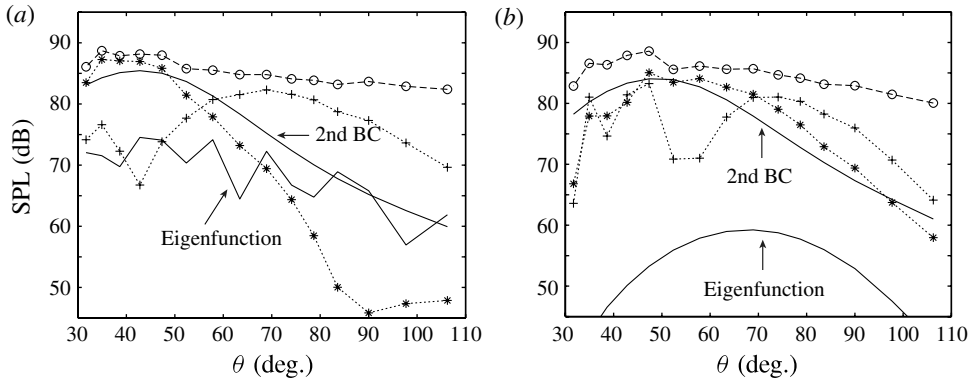
FIGURE 16. Comparison of the SPLs for the azimuthal modes at the mid-field acoustic-array positions: (*a*) $m = 1$, (*b*) $m = 2$. Conditions and symbols are the same as figure 15. Projection of the eigenfunction is computed with the boundary values at $r_0/D = 1$.
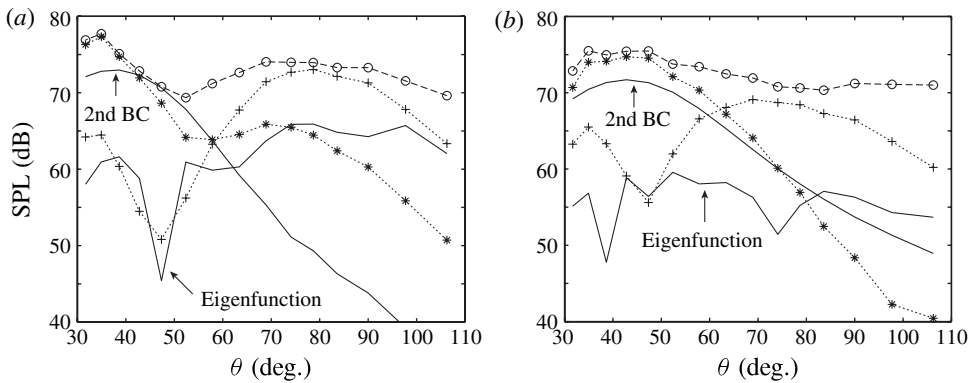

FIGURE 17. Comparison of the SPLs for $M_\infty = 0.5$ at the mid-field acoustic-array positions: (*a*) $m = 0$, (*b*) $m = 1$. Symbols and condition ($St = 0.35$) are the same as figures 15 and 16.

downstream sound, and only the second boundary condition approximately predicts its SPL. To be precise, the directivity becomes sharper with increasing Mach number. Furthermore, the second POD mode mainly occupies the geometrical field. For SP7, we observed contamination of unexpected disturbance in the most upstream ring (Suzuki & Colonius 2006); hence, the hydrodynamic-array data at a slightly downstream position are processed (see figure 3). In turn, the least-squares fitting of the pressure disturbances with the Gaussian profile is not as good as those of other cases (not shown). This may cause some under-prediction in figure 18, although we generally expect better agreement of the SPL at higher Mach numbers.

At a lower frequency in figure 19, the second boundary condition over-predicts the SPL of the axisymmetric mode for an unknown reason; however, the rest of the trends are still the same. As the frequency is increased, the contribution of sound associated with instability waves appears to be concentrated at downstream angles in figure 20. This can be observed from the prediction based on the second boundary condition as well as the first POD mode of the acoustic array. This feature is understandable
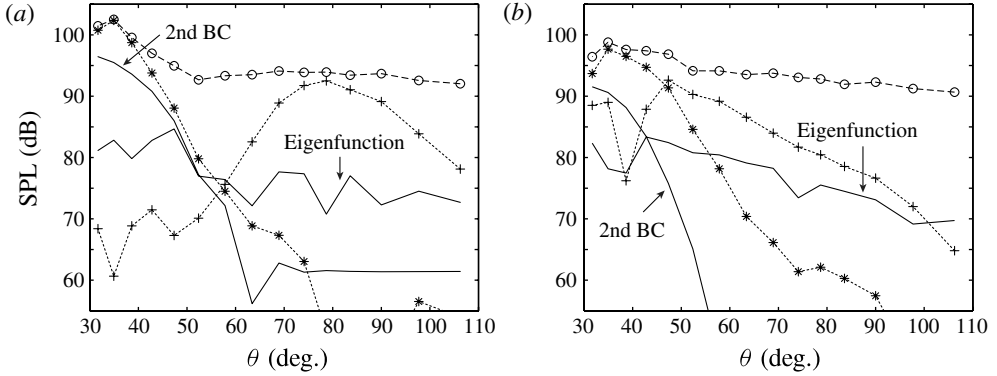
FIGURE 18. Comparison of the SPLs for $M_\infty = 0.9$ at the mid-field acoustic-array positions: (*a*) $m = 0$, (*b*) $m = 1$. Symbols and condition ($St = 0.35$) are the same as figures 15 and 16.
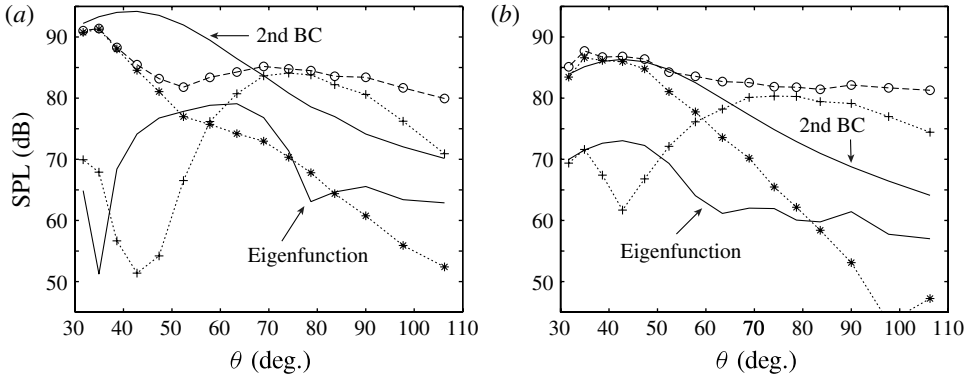

FIGURE 19. Comparison of the SPLs for $St = 0.25$ at the mid-field acoustic-array positions: (*a*) $m = 0$, (*b*) $m = 1$. Symbols and condition ($M_\infty = 0.70$) are the same as figures 15 and 16.

since the correlated length scale of a wave-packet should be reduced with increasing frequency. In addition, the peak SPL is slightly under-predicted for each *m*, probably because the measured level is elevated by sound components other than instability waves. In fact, the directivity of the auto-correlation is smeared at higher frequencies.

The analysis above signifies that the most energetic coherent mode (i.e. the first POD mode) in the acoustic field appears to represent sound associated with instability waves, and the second boundary condition predicts its peak SPL and directivity much better than the first and third boundary conditions. Compared with Reba *et al.* (2005), the projection from the second boundary condition here is analogous to their approach: their approach models the full cross-spectral matrix using the Gaussian profiles, while the current method takes into account the spreading angle of the array and vectorizes pressure signals. This may have improved the recovery of the peak SPL in this study. Reba *et al.* (2008) later included the spreading angle in a robust manner and successfully predicted the SPL at higher Mach numbers. Their approach simulates the full ranks of the cross-spectral matrix, but the current method retains only a single rank and cannot carry other uncorrelated signals. As a result, the second boundary
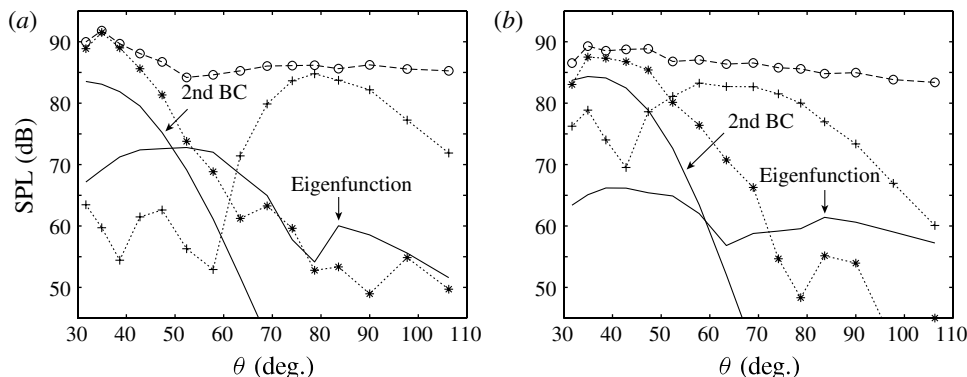
FIGURE 20. Comparison of the SPLs for $St = 0.5$ at the mid-field acoustic-array positions: (*a*) $m = 0$, (*b*) $m = 1$. Symbols and condition ($M_\infty = 0.70$) are the same as figures 15 and 16.

condition only captures the downstream sound, not the entire directivity. The first boundary condition includes growth, saturation and decay due to the shear layer spreading, but ignores nonlinear/non-periodic vortex breakdown beyond the end of the potential core. The third boundary condition represents the most coherent structure in or just outside the shear layer, predominantly capturing linear instability waves.

These results imply that instability waves can generate sound only weakly in the linear regime even including the spreading effects of the shear layer. Once the coherence of hydrodynamic structures breaks beyond the end of the potential core, instability waves start generating significant sound, which is rather coherent in the far field. A few numerical studies (Suponitsky *et al.* 2010; Cavalieri *et al.* 2011) have mentioned this point, but this study experimentally supports it.

5.2. *Source mapping using the acoustic-array data*

We now turn our attention to the source properties of the first two POD modes in the mid-field acoustic array and process them with L_1 generalized-inverse beam-forming, explained in § 4. In the following, a set of figures exhibits the source maps in terms of intensity and phase as well as the recovered directivity of the first two POD modes. The phase evolution expresses the argument of the detected complex sources, $\boldsymbol{a}_1$ and $\boldsymbol{a}_2$, and we plot only the first two dominant multipoles for each POD mode. In addition, each phase plot draws a $1.3a_\infty$ line for reference, which appears to fit well across the conditions below (see appendix B for the interpretation).

Figure 21 shows the results of source mapping for $m = 0$ of SP5 (unheated, $M_\infty = 0.7$) at $St = 0.35$. The first POD mode propagating downstream primarily consists of the $(m, n) = (0, 1)$ mode and extends widely in $0 \lesssim x/D \lesssim 15$ in figure 21(*a*i). The phase evolutions of both $(0, 1)$ and $(0, 2)$ closely follow the phase velocity of $1.3a_\infty$ over the axial distance in figure 21(*b*i). The source distribution in $-5 \leqslant x/D \leqslant 20$ mostly recovers the peak SPL of the sound propagating downstream in figure 21(*c*i), as discussed in § 4.3.

On the other hand, the directivity of the second POD mode is rather omni-directional, as proved in figure 21(*b*/*c*ii). Unlike the first POD mode, both source distribution and phase evolution for the second mode indicate localized source characteristics. The source distribution now comprises $(m, n) = (0, 2)$ and $(0, 0)$, and recovers the directivity almost perfectly. This supports suitability of the free-space multipoles for the reference solutions.
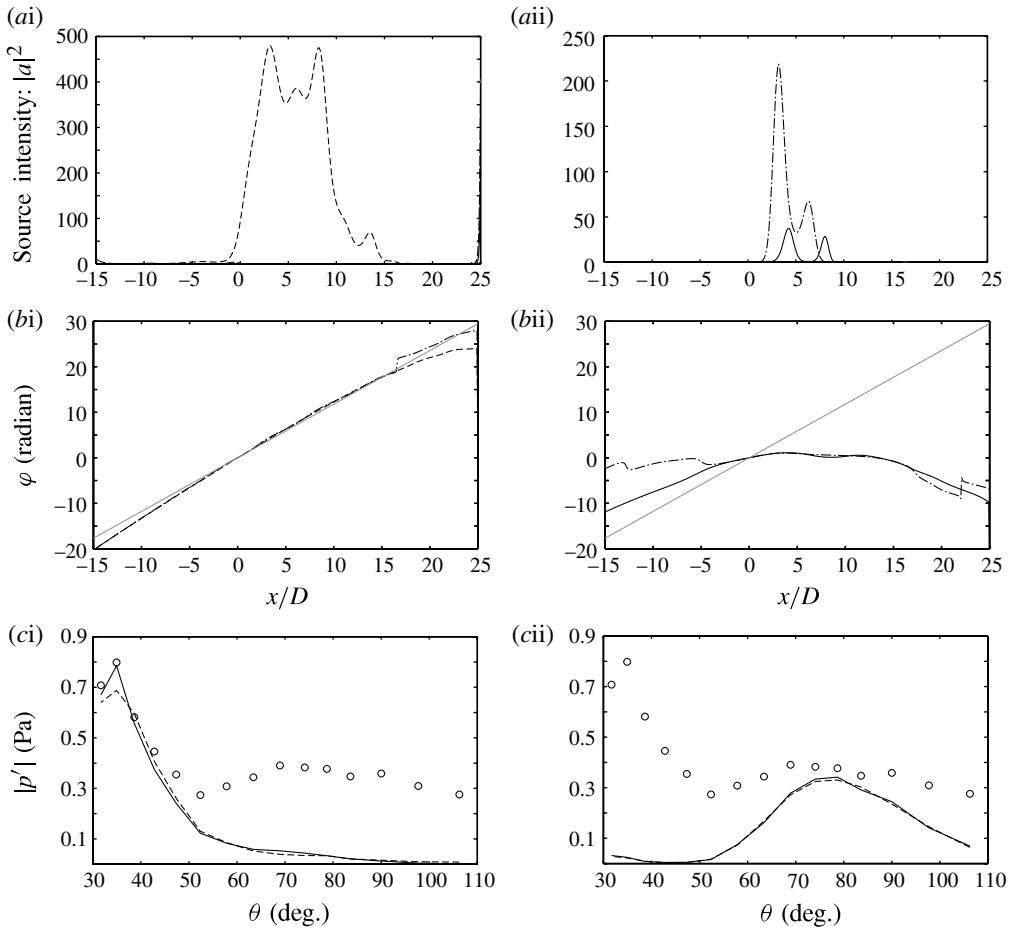
FIGURE 21. Detected source distributions and recovered directivity for SP5 and $m = 0$ at $St = 0.35$. (i) The first POD mode, and (ii) the second POD mode. (*a*) Source maps. Line patterns: ——, $(m, n) = (0, 0)$; $- - -$, $(0, 1)$; $- \cdot - \cdot -$, $(0, 2)$; $\cdots$, $(0, 3)$. (*b*) Phase evolutions of the first two dominant multipoles. Line patterns are the same as above. A straight grey line represents the phase velocity of $1.3a_\infty$. (*c*) Recovered SPL. Symbols: $\circ$, SPL of measured auto-correlation. Line patterns: ——, POD mode to be recovered; $- - -$, recovered SPL from all the multipoles within $-5 \leqslant x/D \leqslant 20$.

Many similarities are found in an azimuthal mode as well. In figure 22, the source maps for $m = 1$ of SP5 at $St = 0.35$ are similarly displayed. The source distribution of the first POD mode is extended axially to a certain extent and dominated by the $(m, n) = (1, 2)$ mode. The phase evolution is aligned well with the reference slope upstream, and it is inclined to lower slopes (i.e. higher phase velocity) downstream. In contrast, the second POD mode is composed of all three modes, and their peaks are formed farther downstream compared with those of $m = 0$. The wavenumbers are clearly lower than the aforementioned slope. The first POD mode captures downstream sound, and the second mode propagates in the geometrical field, as seen for $m = 0$. For both modes, the detected source distributions again recover the SPL fairly well.
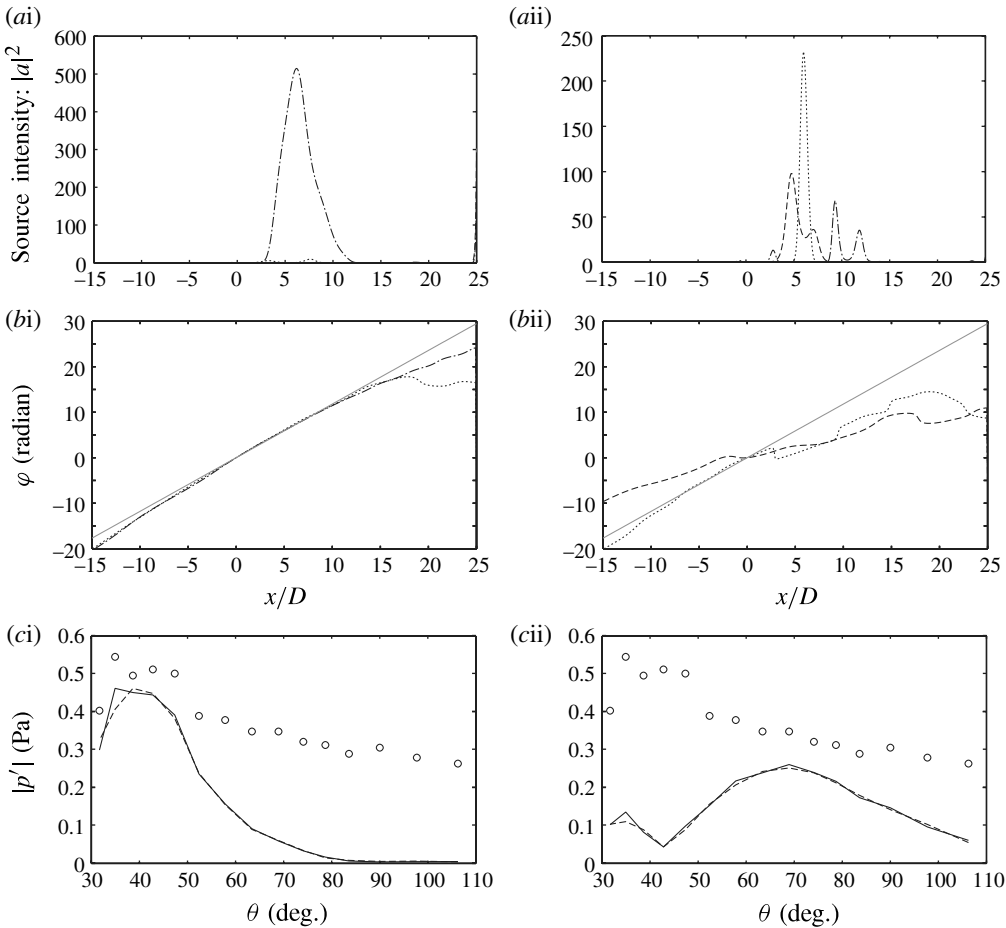
FIGURE 22. Detected source distributions and recovered directivity for SP5 and $m = 1$ at $St = 0.35$. Layout, line patterns and symbols are the same as figure 21, unless otherwise noted. (*a*) Source maps. Line patterns: $- \; - \; -$, $(m, n) = (1, 1)$; $- \cdot - \cdot -$, $(1, 2)$; $\cdots\cdots$, $(1, 3)$. (*b*) Phase evolutions of the first two dominant multipoles. Line patterns are the same as above. A straight grey line represents the phase velocity of $1.3a_\infty$. (*c*) Recovered SPL.

For $m = 2$ of SP5 at $St = 0.35$ (not shown), the first POD mode indicates the localized source properties with $(m, n) = (2, 2)$ as the primary multipole. We find no POD mode clearly capturing the downstream sound possibly because of lower microphone counts in the downstream five rings.

Even if the Mach number varies to $M_\infty = 0.5$ for SP3 or $M_\infty = 0.9$ for SP7 (both at $St = 0.35$), the trends observed above remain the same (plots are omitted): the dominant multipoles detected from the first and second POD modes are identical to those at $M_\infty = 0.7$ for both $m = 0$ and 1 (the only exception is that for $m = 1$ at $M_\infty = 0.9$, the mode corresponding to the aforementioned second mode actually appears in the third POD mode). In the first mode, the source distribution is again axially extended, and its phase evolution is also fitted well with the phase velocity of $1.3a_\infty$ for $m = 0$ and slightly higher for $m = 1$. On the other hand, the source distribution of the second mode is localized as seen above. The downstream sound
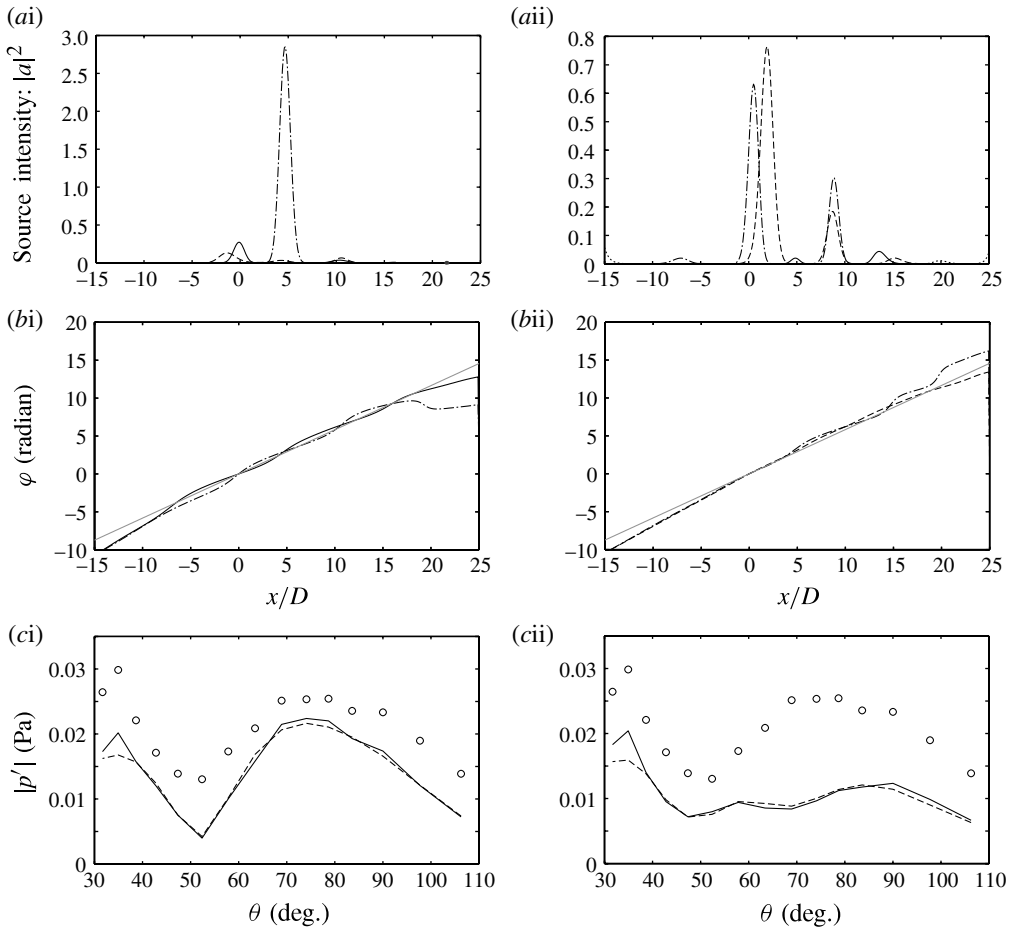
FIGURE 23. Detected source distributions and recovered directivity for SP1 and $m = 0$ at $St = 0.35$. Layout, line patterns and symbols are the same as figure 21. (*a*) Source maps. (*b*) Phase evolutions of the first two dominant multipoles. (*c*) Recovered SPL.

is similarly occupied by the first mode, and the geometrical field predominantly by the second mode. The degrees of agreement in terms of the phase evolution and the recovered SPL are also found to be similar.

When the Mach number decreases to $M_\infty = 0.35$, however, radiation patterns look somewhat different. Figure 23 displays the results of SP1 for $m = 0$ at $St = 0.35$. The first POD mode depicts a two-lobe radiation pattern, and the $(m, n) = (0, 2)$ mode (i.e. quadrupole), which is localized at $x/D \approx 5$, captures such directivity although the phase evolution indicates a wavy character. On the other hand, the second POD mode rather appears to be typical downstream sound, showing decent agreement in terms of the phase evolution and the recovered SPL. Yet, the source distributions create multiple peaks unlike higher-Mach-number cases.

Here, we should mention the interpretation of the source maps. It is still unclear whether detailed source distribution captures precise structures. For example, figure 23(*a*ii) depicts double peaks of the $(m, n) = (0, 1)$ and $(0, 2)$ modes. Although these peaks may actually represent four (or two sets of) distinctive sources, it is
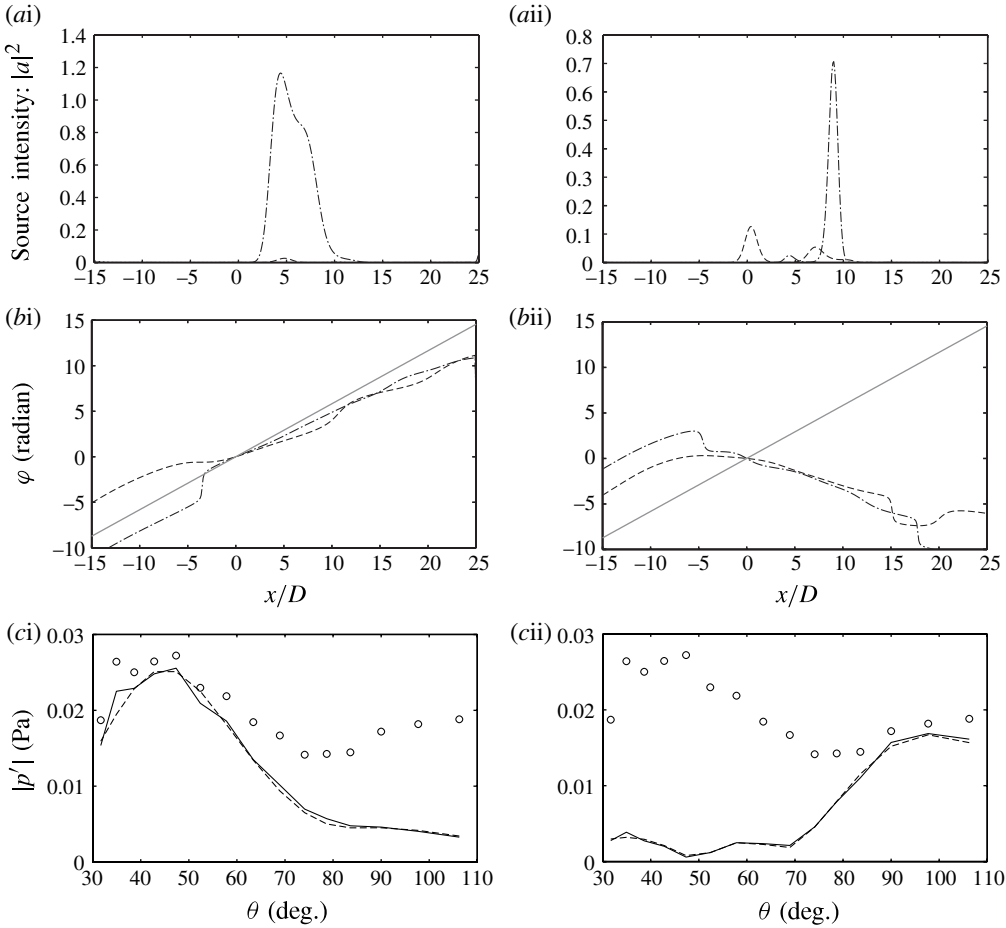
FIGURE 24. Detected source distributions and recovered directivity for SP1 and $m = 1$ at $St = 0.35$. Layout, line patterns and symbols are the same as figure 22. (*a*) Source maps. (*b*) Phase evolutions of the first two dominant multipoles. (*c*) Recovered SPL.

possible that their combination simply forms specific directivity at the mid-field array position. In particular, because these source distributions represent a single POD (i.e. coherent) mode and the phase evolution shows relatively smooth variation in the region of high intensity, it is less likely that each peak captures an individual noise source.

For $m = 1$ at $M_\infty = 0.35$, the first POD mode now captures the downstream sound again, and the second POD mode propagates upstream in figure 24. Moreover, the source property of the first mode indicates a wavy structure, while that of the second mode appears to be localized-source distributions. The only difference from other conditions is that the slope of the primary mode, $(m, n) = (1, 2)$, in figure 24(*bi*) is exceptionally lower than the reference slope. This may be due to a very wide lobe near the peak angle downstream. It is interesting to note that at $M_\infty = 0.35$, quadrupoles are dominant for both $m = 0$ and $m = 1$, as well as $m = 2$ (not shown). Similar trends have been reported at low Mach numbers in Suzuki (2006) and Lee & Bolton (2007).
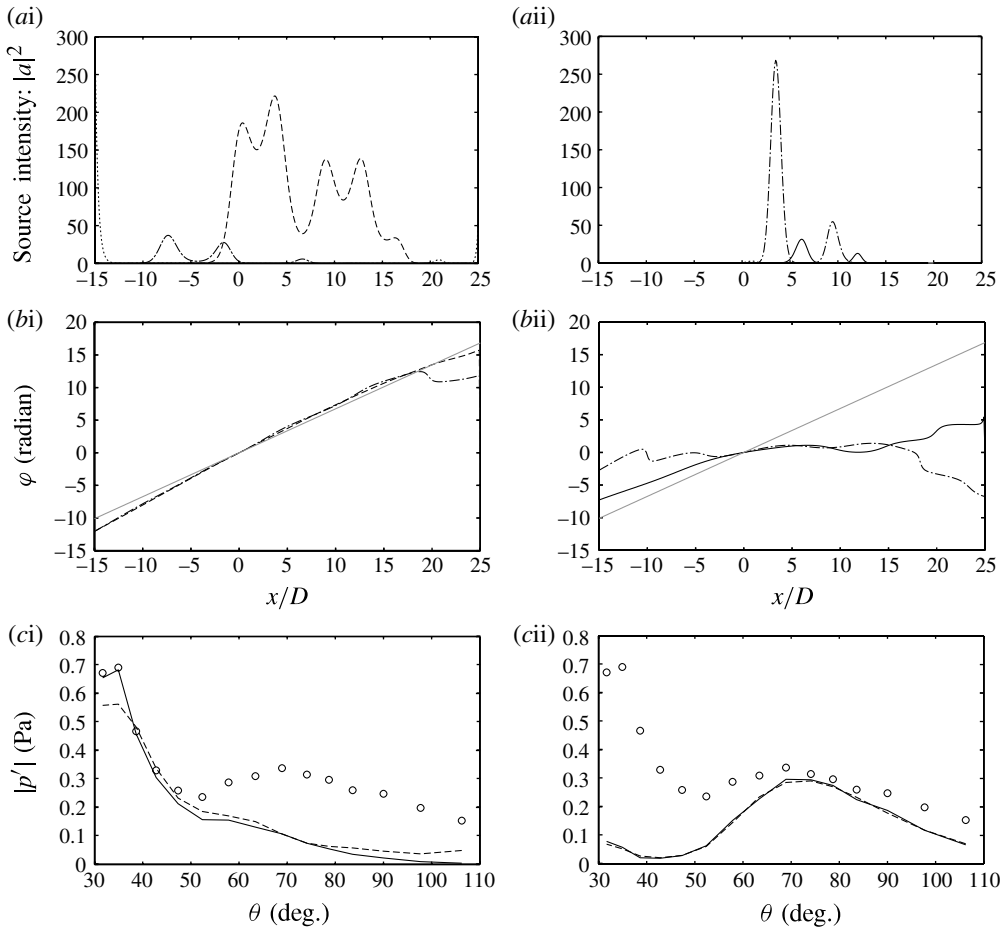
FIGURE 25. Detected source distributions and recovered directivity for SP5 and $m = 0$ at $St = 0.20$. Layout, line patterns and symbols are the same as figure 21. (*a*) Source maps. (*b*) Phase evolutions of the first two dominant multipoles. (*c*) Recovered SPL.

As the frequency decreases ($St = 0.20$ for SP5 and $m = 0$), figure 25 indicates that the apparent source distributions slightly diffuse, but the detected multipoles and the radiation characteristics are still the same as those at $St = 0.35$ for both POD modes. Moreover, the phase evolution of the first POD mode depicts a constant slope quite extensively. The recovered directivity is slightly short at the peak SPL since some spurious sources are created upstream.

For the $m = 1$ mode at $St = 0.20$ in figure 26, the first POD mode, which captures the downstream sound, is again detected as $(m, n) = (1, 2)$, and its wavenumber is also aligned well with the slope of $1.3a_\infty$. The second POD mode is now primarily composed of the $(1, 1)$ mode as opposed to the $(1, 3)$ mode at $St = 0.35$, and the SPL peak is found nearly at $90°$.

Even at a higher frequency ($St = 0.60$ for SP5 and $m = 0$), major characteristics remain the same for both POD modes. A minor difference is that the source distributions tend to be concentrated upstream in figure 27(*a*i/ii) compared to lower Strouhal numbers, and this trend is common to $m = 1$ in figure 28. More importantly,
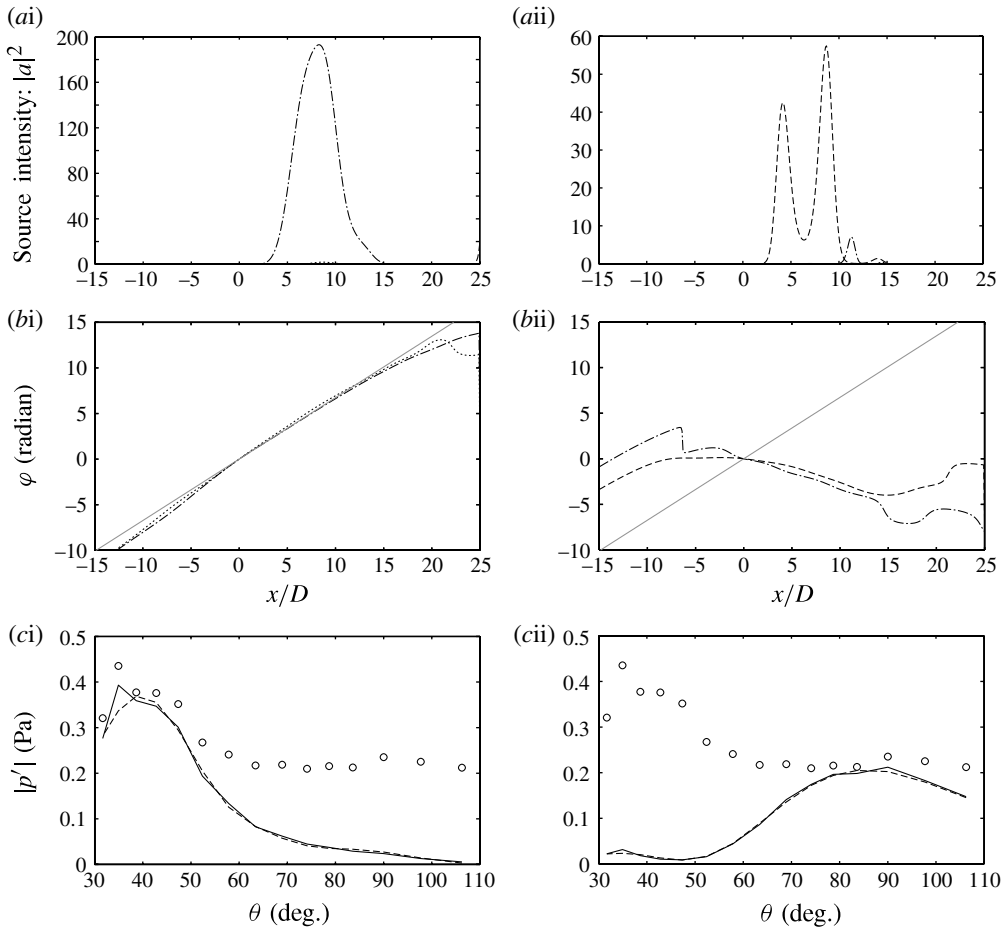
FIGURE 26. Detected source distributions and recovered directivity for SP5 and $m = 1$ at $St = 0.20$. Layout, line patterns and symbols are the same as figure 22. (*a*) Source maps. (*b*) Phase evolutions of the first two dominant multipoles. (*c*) Recovered SPL.

the recovered SPL still captures the directivity of the POD mode well for both $m = 0$ and $m = 1$, while refraction could be more relevant at higher frequencies. These two distinctive source features can be observed as high as $St = 1.0$ (not shown) although the source detection starts to be disrupted by spurious downstream sources.

The results in this section consistently demonstrate that the primary coherent signal (i.e. the first POD mode) in the acoustic array represents sound propagating downstream except at $M_\infty = 0.35$ for $m = 0$, and the secondary mode generally occupies the geometrical field. This may suggest two independent sound-generation mechanisms, as proposed by Tam (Tam *et al.* 1996; Tam & Auriault 1999). The source distribution of the former mode spreads axially, while the latter tends to be localized. These noise sources are decomposed well by the free-space multipoles for both $m = 0$ and $m = 1$ over ranges of the Mach numbers and Strouhal numbers. Hence, it is probably appropriate to model the radiation patterns, particularly for the downstream sound, by treating the noise sources globally rather than regarding them as a collection of point sources with refraction, at least up to $St \lesssim 0.6$.
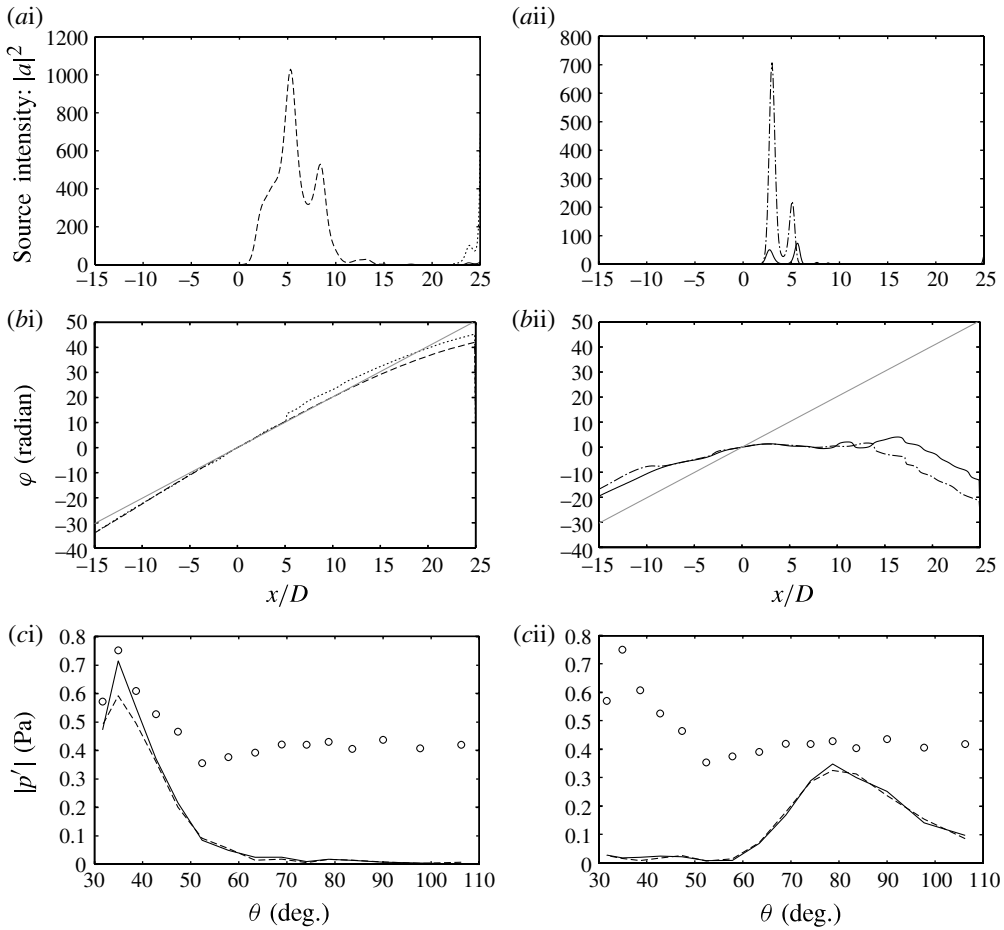
FIGURE 27. Detected source distributions and recovered directivity for SP5 and $m = 0$ at $St = 0.60$. Layout, line patterns and symbols are the same as figure 21. (*a*) Source maps. (*b*) Phase evolutions of the first two dominant multipoles. (*c*) Recovered SPL.

In contrast, the source model for the sound in the geometrical field remains uncertain. As mentioned in § 4.3, both free-space and high-frequency asymptotic multipoles can recover the measured SPL equally well. Hence, there exists a possibility that multipole point sources with refraction suitably express the sound property of this type, though quadrupoles may not be necessarily most representative (except at low Mach numbers). Although Tam and his colleagues attributed the mechanism of this noise component to fine-scale turbulence, it is unclear whether 'fine-scale' is an appropriate term to express this source mechanism because the second POD mode still retains strong coherence.

It should be remembered that in cross-spectral matrices of the hydrodynamics array, we can hardly find POD modes with clear supersonic phase velocity. The phase velocity of the primary POD mode along the hydrodynamic array typically starts at $\sim 0.6 u_{jet}$ or higher from the nozzle exit and ends at $\sim u_{jet}$ downstream (i.e. from pure hydrodynamic to a mixture of hydrodynamic and acoustic disturbances). In contrast, the phase velocity of the first POD mode detected from the acoustic array
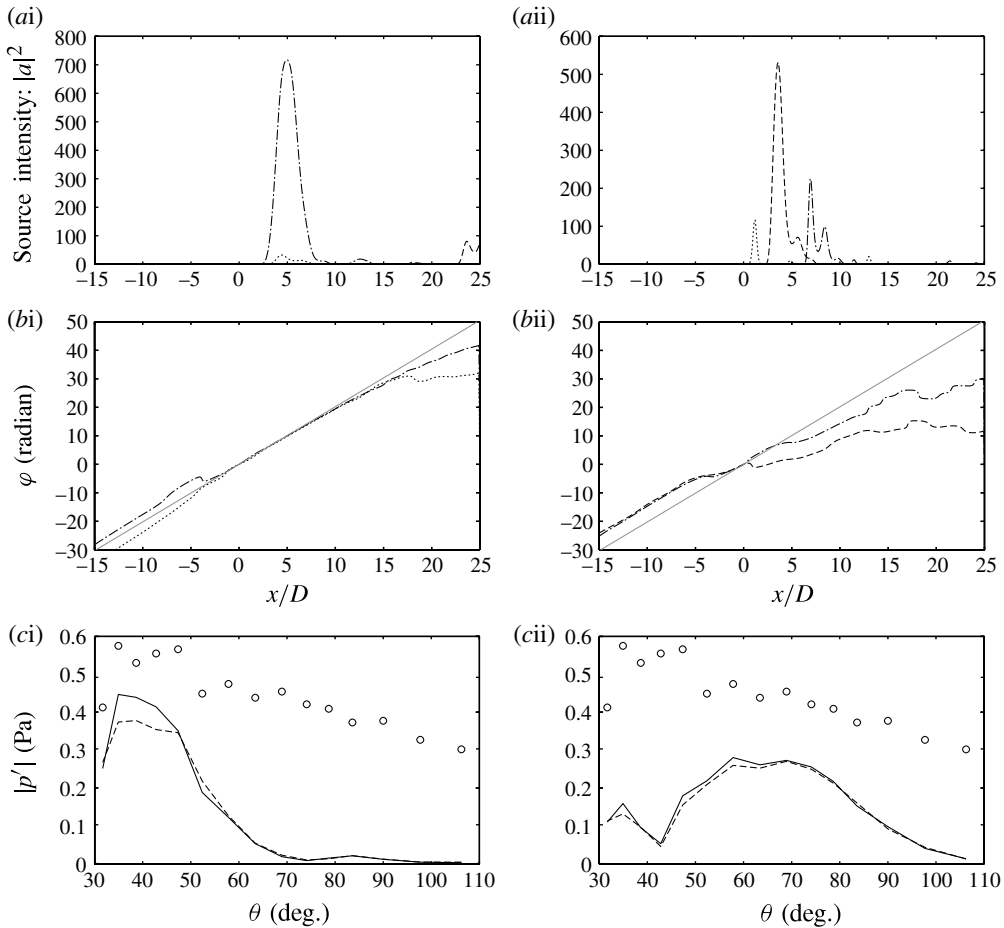
FIGURE 28. Detected source distributions and recovered directivity for SP5 and $m = 1$ at $St = 0.60$. Layout, line patterns and symbols are the same as figure 22. (*a*) Source maps. (*b*) Phase evolutions of the first two dominant multipoles. (*c*) Recovered SPL.

appears $\sim 1.3 a_\infty$. Figure 29 plots an example of phase evolutions of all the POD modes, taken from SP5 at $St = 0.35$. Only limited numbers of downstream stations of the fifth mode for $m = 0$ and the third and fourth modes for $m = 1$ appear to exceed the sonic phase velocity. It is understandable that the hydrodynamic-pressure fluctuations overcome the acoustic signals and the orthogonal constraint makes the structures of higher POD modes opaque. In fact, the envelopes of these modes are not smooth enough to project into the acoustic field.

On the other hand, the second boundary condition, which simulates the local phase relation of adjacent microphone rings, tends to recover the SPL at the acoustic-array position in § 5.1. This implies that acoustic signals start to overcome hydrodynamic fluctuations downstream. We have actually observed that the averaged phase velocity starts increasing toward the end of the hydrodynamic array in figures 4(*b*) and 5(*b*). Referring to appendix B and the detected phase velocity of the first POD mode throughout this section, we may be able to conclude that the phase velocity of the
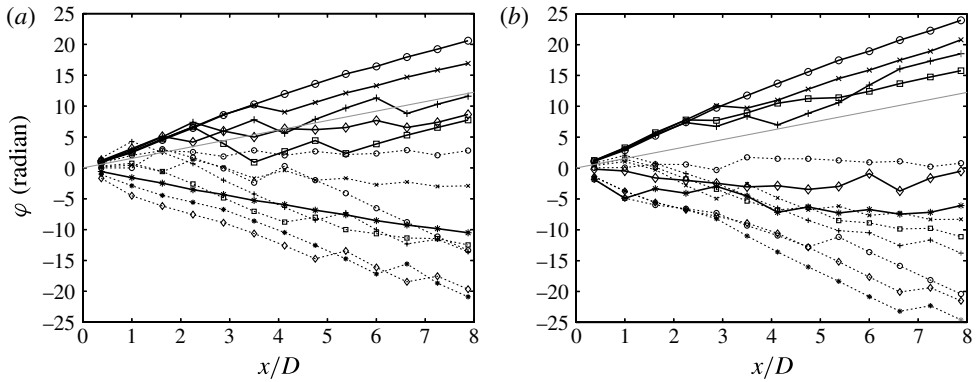
FIGURE 29. Phase evolutions of all the POD modes along the hydrodynamic array (SP5 at $St = 0.35$): (*a*) $m = 0$, (*b*) $m = 1$. Symbols: $- \circ -$, first POD mode; $- \times -$, second; $-\square-$, third; $- + -$, fourth; $- \diamond -$, fifth; $- * -$, sixth; dotted lines for the rest of the higher modes; the thin grey line is the slope representing the sonic line.

actual source can reach about $\sim u_{jet}$ and the collapse of the potential core forms a wave-packet, resulting in supersonic phase velocity.

6. Conclusions

Properties of coherent noise from a subsonic round jet have been investigated by post-processing two types of phased-microphone array data, one being from a mid-field array acquiring acoustic signals and the other from a near-field array measuring hydrodynamic pressure disturbances. Focusing on relatively low frequencies ($0.2 \lesssim St \lesssim 0.6$), the downstream sound and the sound in the rest (i.e. geometrical field) have been analysed, and representative jet-noise-source models, namely those associated with instability waves and multipole noise sources, have been evaluated.

To elucidate the relation between instability waves and downstream sound, near-field pressure signals have been projected to the acoustic-array position via a boundary-value problem. Three types of boundary conditions have been examined: (i) an eigenfunction is computed based on linear stability analysis at each axial station assuming a locally parallel flow, and the axial wavenumber is integrated; (ii) the SPL measured at each microphone ring of the hydrodynamics array is connected based on the phase relation between adjacent rings; (iii) from a cross-spectral matrix of the hydrodynamic array, the first POD mode is extracted. Projections with the first and third boundary conditions substantially under-estimate the SPL measured at the acoustic array, and only the second boundary condition can recover it at an equivalent level at downstream angles. In fact, the directivity obtained from the second boundary condition shows similarity to the first POD mode in the acoustic array. The wave-packet envelope of the second boundary condition decays more slowly beyond the end of the potential core, and its phase velocity is faster than the other two boundary conditions. Namely, collapse of coherent structures at the end of the potential core probably causes these differences, resulting in the dominant sound generation. The envelope of an eigenfunction, which grows, saturates and decays merely due to the spreading shear layer, is clearly insufficient to produce the actual SPL; hence, nonlinearity and non-periodicity may be necessary.

While the first POD mode of the acoustic array dominates sound downstream, the second POD mode generally occupies the geometrical acoustic field, which is outside the zone of silence. The only exception is the acoustic field at $M_\infty = 0.35$, in which quadrupoles appear to be dominant and the first POD mode for $m = 0$ indicates a multi-lobe radiation pattern. Since the POD modes are orthogonal to each other, the sound-generation mechanisms of the aforementioned two modes are most likely independent of each other. Moreover, both modes exhibit fairly strong coherence over the zenithal angles in the acoustic field. Compared to the clear relation between the hydrodynamic coherent structures and the downstream sound, a suitable representation for the sound sources responsible in the geometrical field remains unclear.

Noise sources radiating these two types of POD modes have been localized using L_1 generalized-inverse beam-forming. Its unique capability of phase detection is found to be useful for identification of the source properties. In both axisymmetric and first azimuthal modes, the first POD mode has been clearly identified as an extensive wavy structure with nearly a constant wavenumber, which is most likely associated with instability waves. Moreover, their radiation patterns can be decomposed by the free-space multipoles better than by the high-frequency asymptotic Green's functions, indicating a negligible impact of refraction at $St \leqslant 0.6$. In contrast, the noise sources of the second POD mode tend to be more localized, and this is consistent with the spreading-radiation pattern in the geometrical field. These results seem to support two independent sound-generation mechanisms, proposed by Tam (Tam *et al.* 1996; Tam & Auriault 1999).

Acknowledgements

Appendix A. Procedure of L_1 generalized-inverse beam-forming

The beam-forming procedure introduced in §4.2 is itemized below.

(i) Generate a cross-spectral matrix and perform the eigenvalue decomposition.

(ii) Generate the specified number of the POD modes which are composed of the eigenvalue and its eigenvector.

(iii) Define the source types and the target domain, calculate a transfer function from a complex source distribution to signals at the microphones, and store it.

(iv) Compute the initial distribution of a_i based on a least-squares technique for an under-determined generalized-inverse problem (i.e. $N_{mic} < N_{type} \times N_{grid}$) as

$$a_i \approx A^\dagger (A A^\dagger + \epsilon I)^{-1} v_i. \tag{A 1}$$

(v) Increase the resolution of the map by iteratively solving a_i with

$$a_i^{(n+1)} = W_i^{(n)} A^\dagger (A W_i^{(n)} A^\dagger + \epsilon I)^{-1} v_i, \tag{A 2}$$

where $W_i^{(n)}$ is an $N_{type} \times N_{grid}$ by $N_{type} \times N_{grid}$ diagonal matrix whose components are given by $w = |a_i^{(n)}|$, the superscript (n) being the iteration counter.
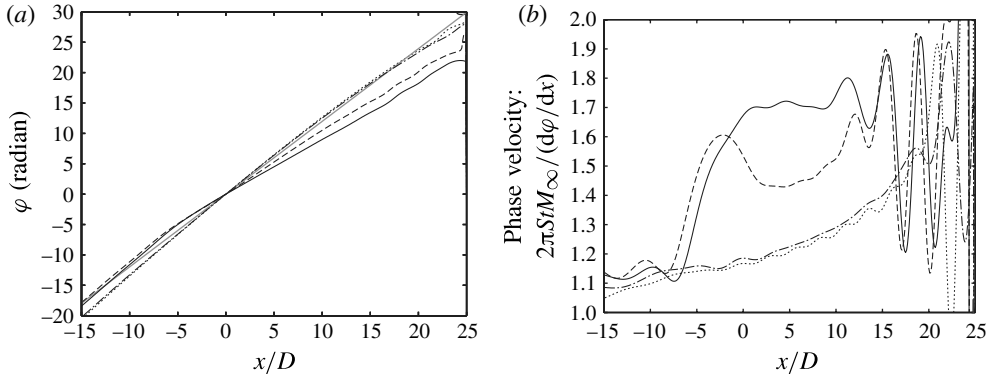
FIGURE 30. Detected phase evolutions for different imposed phase velocities (model-source profile for SP5 and $m = 0$ at $St = 0.35$). Line patterns of the original phase velocity: $\cdots\cdots$, $0.75a_\infty$; $-\cdot-\cdot-$, $1.0a_\infty$; $-~-~-$, $1.25a_\infty$; and $\underline{\qquad}$, $1.5a_\infty$ for both figures. (*a*) Phase evolution. The thin grey line denotes the phase velocity corresponding to $1.3a_\infty$. (*b*) Phase velocity.

(vi) Repeat (v) for all *i* until the iteration counter reaches the designated number or the L_1 norm (4.4) starts increasing.

(vii) Generate source maps of all the source types for each selected POD mode.

Appendix B. Detected phase velocity in L_1 generalized-inverse beam-forming

To analyse the relation between the original and the detected phase velocities, we impose the same Gaussian profile adopted in § 4.2 (i.e. the second boundary condition in figure 5*a*), but with four different constant phase velocities ($0.75a_\infty$, $1.0a_\infty$, $1.25a_\infty$ and $1.5a_\infty$). In all four cases, the sound propagates predominantly downstream, and the algorithm detects the $(m, n) = (0, 1)$ mode to be the primary multipole. We only focus on the phase evolution of this primary mode here, especially in $0 \lesssim x/D \lesssim 10$, in which the source distribution is concentrated.

Figures 30(*a*) and 30(*b*) plot the phase evolutions and the phase velocity, respectively, for all four cases. For reference, a straight grey line indicates the slope of $1.3a_\infty$ in figure 30(*a*). While the imposed phase velocity is sonic or less, the detected phase-velocity profile remains nearly the same, roughly starting with $\sim 1.1a_\infty$ and ending with $\sim 1.3a_\infty$ at $x/D \approx 10$. Once the original phase velocity becomes supersonic, the detected one correspondingly increases. Thus, the detected phase velocity of the wavy-type source seems to be always supersonic and higher than the original phase velocity.

Appendix C. Multipoles for asymptotic Green's functions

C.1. *Construction of asymptotic solutions*

The procedure to derive the multipoles of the asymptotic Green's functions used in § 4.3 is explained below. Following the notation in § 3.1, logarithmic pressure distribution is Fourier-transformed as

$$\hat{\Pi}(\omega, k_x, r, m) \equiv \frac{1}{(2\pi)^3} \int \int \int \frac{1}{\gamma} \log\left(\frac{p}{p_\infty}\right) \exp[i(\omega t - k_x x - m\phi)] \, dt \, dx \, d\phi. \quad (C\,1)$$

When the mean flow can be assumed axisymmetric and locally parallel in the axial direction, pressure fluctuations are governed by the third-order convective wave equation (Pridmore-Brown 1958; Lilley 1974), which can also be Fourier-transformed as (Goldstein 1976)

$$n^2 \frac{\partial}{\partial r}\left(\frac{r}{n^2}\frac{\partial \hat{\Pi}}{\partial r}\right) + \left[n^2 - k_x^2 - \frac{m^2}{r^2}\right] r\hat{\Pi} = \frac{r\delta(r - r_{src})}{r_{src}a^2}, \tag{C 2}$$

where the delta function indicates the radial position of a ring source r_{src}, which is included in the denominator to keep the total source strength independent of the source location, and a denotes the local speed of sound. Here, the effective index of refraction $n(r) \equiv (\omega - k_x u_x)/a$ differs from the zenithal-mode number of the associated Legendre function in (4.1). At high frequencies, it is convenient to recast the dependent variable as $\hat{\Pi}^\bullet \equiv \hat{\Pi}/n$ and to rewrite (C 2) as

$$\frac{\partial^2 \hat{\Pi}^\bullet}{\partial r^2} + \frac{1}{r}\frac{\partial \hat{\Pi}^\bullet}{\partial r} + \left[n^2 - k_x^2 - \frac{m^2}{r^2}\right]\hat{\Pi}^\bullet$$

$$+ \left[\frac{1}{n}\frac{\partial^2 n}{\partial r^2} + \frac{1}{nr}\frac{\partial n}{\partial r} - 2\left(\frac{1}{n}\frac{\partial n}{\partial r}\right)^2\right]\hat{\Pi}^\bullet = \frac{\delta(r - r_{src})}{r_{src}a^2 n}. \tag{C 3}$$

The transformation above is similar to one by Goldstein (1976), but the resulting expression retains the form of the Bessel equation with a variable index. In the high frequency limit, the inside the brackets of the fourth term on the left-hand side vanishes relative to that of the third term. We should note that $r^{-1}\partial n/\partial r$ inside the brackets of the fourth term stays $O(1)$ or smaller as $r \to 0$ by imposing $\partial u_x/\partial r = 0$ at $r = 0$ (i.e. $\partial n/\partial r \to 0$).

To construct the asymptotic solutions for (C 3), we consider a pair of fundamental solutions that satisfy the boundary conditions of

$$\hat{\Pi}^\bullet \sim r^{|m|} \quad \text{as } r \to 0, \tag{C 4a}$$

$$\hat{\Pi}^\bullet \sim r^{-1/2}\exp\left[ir\sqrt{(\omega/a_\infty)^2 - k_x^2}\right] \quad \text{as } r \to \infty. \tag{C 4b}$$

Following Wundrow & Khavaran (2004), we take

$$\hat{\Pi}^\bullet \sim \begin{cases} J_m(\tilde{r}), & 0 \leqslant r < r_{src}, \\ H_m^{(1)}(\tilde{r}), & r_{src} < r < \infty, \end{cases} \tag{C 5}$$

where $\tilde{r} \equiv \int_0^r \sqrt{n^2 - k_x^2}\,dr$ for those solutions. They are still approximate in the sense that $\tilde{r} \approx r\sqrt{n^2 - k_x^2}$, which is valid only for $r \ll a/\omega$.

To connect these solutions across the source under the approximation above, it is convenient to rewrite (C 3) in the form of a one-dimensional wave equation:

$$\frac{\partial^2(\tilde{r}^{1/2}\hat{\Pi}^\bullet)}{\partial \tilde{r}^2} + \left[1 - \frac{m^2 - (1/2)^2}{r^2(n^2 - k_x^2)}\right](\tilde{r}^{1/2}\hat{\Pi}^\bullet) \approx \frac{\delta(r - r_{src})}{\tilde{r}_{src}^{1/2}a^2 n\sqrt{n^2 - k_x^2}}. \tag{C 6}$$

The solution for (C 6) in $r_{src} < r < \infty$ can be found as

$$\hat{\Pi}(\omega, k_x, r, m) \equiv n\hat{\Pi}^\bullet \approx \frac{J_m\left(\int_0^{r_{src}}\sqrt{n^2 - k_x^2}\,dr\right)}{W(\tilde{r}_{src})a_{src}^2 n_{src}\sqrt{n_{src}^2 - k_x^2}}H_m^{(1)}\left(\int_0^r\sqrt{n^2 - k_x^2}\,dr\right). \tag{C 7}$$

The Wronskian above is defined as

$$W(\tilde{r}) \equiv \frac{\partial(\tilde{r}^{1/2}\mathrm{H}_m^{(1)})}{\partial\tilde{r}}(\tilde{r}^{1/2}\mathrm{J}_m) - \frac{\partial(\tilde{r}^{1/2}\mathrm{J}_m)}{\partial\tilde{r}}(\tilde{r}^{1/2}\mathrm{H}_m^{(1)}), \tag{C 8}$$

which is constant with respect to r_{src} from (C 6). By taking the limit of $r_{src} \to 0$ as well as $\omega r/a \to \infty$ and the inverse Fourier transform with respect to k_x, the monopole directivity can be recovered for $m = 0$ with the stationary-phase method.

To calculate the multipoles, (C 7) is differentiated with respect to the source coordinates. For the radial derivative, it is convenient to expand the Bessel function about the jet axis as

$$\mathrm{J}_m(\tilde{r}) = \sum_{l=0}^{\infty} \frac{(-1)^l}{l!\,\Gamma(l+m+1)}\left(\frac{\tilde{r}}{2}\right)^{2l+m}, \tag{C 9}$$

where Γ denotes the gamma function. This indicates, for example, that J_0, J_0'', $\mathrm{J}_0^{(4)}$, ... take non-zero values, and each differentiation with r produces $-\mathrm{i}\sqrt{n^2 - k_x^2}$ as $r \to 0$. Although this is accurate only at the jet axis, we regard this factor as the radial derivative due to the simplification of sources located along jet axis for beam-forming. In addition, we take $u_{src} = 0.5u_{jet}$ to compute n_{src} assuming that the actual sources are generated in the middle of the shear layer. For the axial derivative, on the other hand, $-\mathrm{i}k_x$, which is the same factor as the free space, is multiplied according to the parallel-flow assumption.

These multiplication factors, $-\mathrm{i}k_x$ and $-\mathrm{i}\sqrt{n_{src}^2 - k_x^2}$, correspond to $-\mathrm{i}(\omega/a)\cos\theta$ and $-\mathrm{i}(\omega/a)\sin\theta$, respectively, in the free-space multipoles given by (4.1). To be precise, the coefficients are normalized such that the integral over the entire sphere is set to be equal for all the modes. Considering that these multipoles are distorted in the shear layer, the same coefficients are applied for the multipoles in the jet as well. Although a similar approach for multipoles was introduced by Tester & Morfey (1976), their factors are different from above because of a different limiting process and normalization. Thus, multipoles can be constructed by just multiplying (C 7) with these factors and by extending the propagation paths with ray-tracing explained below.

C.2. *Ray-tracing to account for refraction*

To solve the ray-tracing equations, a set of ordinary differential equations below (see Suzuki & Lele 2002 for notation and derivation) is integrated using the standard fourth-order Runge–Kutta scheme:

$$\frac{\mathrm{d}x_i}{\mathrm{d}t} = \frac{a^2}{1 - u_k\varphi_k}\varphi_i + u_i, \tag{C 10a}$$

$$\frac{\mathrm{d}\varphi_i}{\mathrm{d}t} = -\frac{\partial u_k}{\partial x_i}\varphi_k - \frac{1 - u_k\varphi_k}{2a^2}\frac{\partial a^2}{\partial x_i}, \tag{C 10b}$$

$$\frac{\mathrm{d}\varphi}{\mathrm{d}t} = 1, \tag{C 10c}$$

where φ_i denotes a spatial derivative of the phase with respect to x_i. In the actual computation, only the axial velocity component is fitted with either a hyperbolic tangent profile (in approximately $x/D \lesssim 9$, and the most upstream profile is extended to $x/D < 0$) or a Gaussian profile (in approximately $x/D \gtrsim 9$) at each axial station. From the velocity profile, the temperature profile is again estimated using the Crocco–Busemann relation (Schlichting 1960).
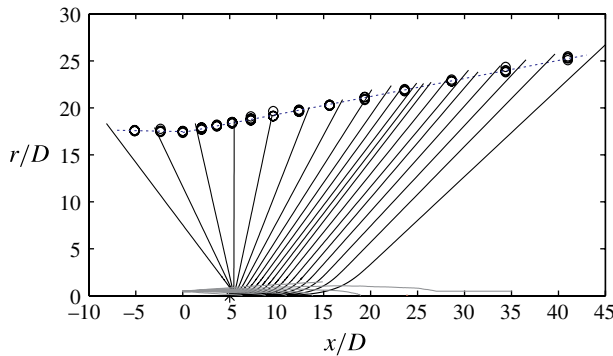
FIGURE 31. Example of ray trajectories computed using the PIV mean-flow data for SP5 (unheated, $M_\infty = 0.7$). The source, marked as $*$, is located at $x/D = 5$, and the microphone positions of the acoustic array are indicated by $\circ$. Mach-number contours ($0 \leqslant M \leqslant 0.7$ with 0.1 increment) are also superimposed with grey lines.

To calculate the amplitude part, $P(\mathbf{x})$, the ray-tube theory is applied. For sheared flows, the Blokhintzev invariant (Blokhintzev 1946),

$$\frac{P^2 S}{1 - u_k \varphi_k} \left| \frac{\mathrm{d}x_i}{\mathrm{d}t} \right| = \text{const.}, \qquad (C\,11)$$

is conserved along a ray tube. To track the area, S, which is normal to the ray direction, four adjacent rays are issued as a single set.

From each candidate source position on the jet axis ($-15 \leqslant x/D \leqslant 25$ with an equal spacing of $2.5D$), 20 sets of such rays are distributed, and their initial zenithal angles are set such that the streamwise extent of the array is fully covered without sparsity. An example of ray trajectories is displayed in figure 31. The arclength, amplitude and local wavenumber are then calculated at the microphone positions by interpolation using four neighbourhood points on the rays. The local wavenumber $\omega \varphi_x$, which is equivalent to k_x, is used to compute the multipole factors discussed above.

We may argue the suitability of the assumption that the sources are localized along the jet axis. Since the substantial part of refraction occurs in the vicinity of the lip line, refraction can be a minor effect for noise sources generated on the outer side of the shear layer. Even in such a case, ray trajectories outside the shear layer are relatively similar so long as the centre of the 'virtual' sources is aligned along the jet axis. The point evaluated in § 4.3 is whether such refracted radiation patterns can recover the measured directivity regardless of the axial source positions. For this purpose, the asymptotic Green's functions derived above should suffice.

REFERENCES

AHUJA, K. K. 1973 Correlation and prediction of jet noise. *J. Sound Vib.* **29** (2), 155–168.

ARMSTRONG, R. R. 1981 Influence on Mach number on coherent structure relevant to jet noise. *AIAA J.* **19** (6), 677–683.

ARNDT, R. E. A., LONG, D. F. & GLAUSER, M. N. 1997 The proper orthogonal decomposition of pressure fluctuations surrounding a turbulent jet. *J. Fluid Mech.* **340**, 1–33.

BLOKHINTZEV, D. I. 1946 The propagation of sound in an inhomogeneous and moving medium. Part 1. *J. Acoust. Soc. Am.* **18** (2), 322–328.

BOYD, J. P. 1985 Complex coordinate methods for hydrodynamic instabilities and Sturm–Liouville eigenproblems with an interior singularity. *J. Comput. Phys.* **57**, 454–471.

BRIDGES, J. & BROWN, C. 2005 Validation of the small hot jet acoustic rig for aeroacoustic research. *AIAA Paper* 2005-2846.

BRIDGES, J., KHAVARAN, A. & HUNTER, C. A. 2008 Assessment of current jet noise prediction capabilities. *AIAA Paper* 2008-2933.

BRIDGES, J. & WERNET, M. 2003 Measurements of the aeroacoustic sound source in hot jets. *AIAA Paper* 2003–3130.

CAVALIERI, A. V. G., JORDAN, P., AGARWAL, A. & GERVAIS, Y. 2011 Jittering wave-packet models for subsonic jet noise. *J. Sound Vib.* **330**, 4474–4492.

CITRINITI, J. H. & GEORGE, W. K. 2000 Reconstruction of the global velocity field in the axisymmetric mixing layer utilizing the proper orthogonal decomposition. *J. Fluid Mech.* **418**, 137–166.

COLONIUS, T., LELE, S. K. & MOIN, P. 1997 Sound generated in a mixing layer. *J. Fluid Mech.* **330**, 375–409.

CRIGHTON, D. G. 1975 Basic principles of aerodynamic noise generation. *Prog. Aerosp. Sci.* **16**, 31–96.

CRIGHTON, D. G. & HUERRE, P. 1990 Shear-layer pressure fluctuations and superdirective acoustic sources. *J. Fluid Mech.* **220**, 355–368.

CROW, S. C. & CHAMPAGNE, F. H. 1971 Orderly structure in jet turbulence. *J. Fluid Mech.* **48**, 547–591.

DOUGHERTY, R. P. 2012 Improved generalized inverse beamforming for jet noise. *Intl J. Aeroacoust.* **11** (3–4), 259–290.

DOWLING, A. P., FFOWCS WILLIAMS, J. E. & GOLDSTEIN, M. E. 1978 Sound production in a moving stream. *Phil. Trans. R. Soc. Lond.* A **288**, 321–349.

DURBIN, P. A. 1983 High frequency Green function for aerodynamic noise in moving media. Part 1. General theory. *J. Sound Vib.* **91** (4), 519–525.

FARANOSOV, G. A. & KOPIEV, V. F. 2009 Localization of sound sources by means of ADT data interpretation improved by refraction effect consideration. *AIAA Paper* 2009-3215.

FFOWCS WILLIAMS, J. E. 1963 The noise from turbulence convected at high speed. *Phil. Trans. R. Soc. Lond.* A **254**, 469–503.

FFOWCS WILLIAMS, J. E. & KEMPTON, A. J. 1978 The noise from the large-scale structure of a jet. *J. Fluid Mech.* **84**, 673–694.

GOLDSTEIN, M. E. 1976 *Aeroacoustics*. McGraw-Hill.

GOLDSTEIN, M. E. 1982 High frequency sound emission from moving point multipole sources embedded in arbitrary transversely sheared mean flows. *J. Sound Vib.* **80** (4), 499–522.

GOLDSTEIN, M. E. 2003 A generalized acoustic analogy. *J. Fluid Mech.* **488**, 315–333.

GOLDSTEIN, M. E. 2011 Recent developments in the application of the generalized acoustic analogy to jet noise prediction. *Intl J. Aeroacoust.* **10** (2–3), 89–116.

GOLDSTEIN, M. E. & LEIB, S. J. 2005 The role of instability waves in predicting jet noise. *J. Fluid Mech.* **525**, 37–72.

GUDMUNDSSON, K. & COLONIUS, T. 2011 Instability wave models for the near-field fluctuations of turbulent jets. *J. Fluid Mech.* **689**, 97–128.

HILEMAN, J. I., THUROW, B. S., CARABALLO, E. J. & SAMIMY, M. 2005 Large-scale structure evolution and sound emission in high-speed jets: real-time visualization with simultaneous acoustic measurements. *J. Fluid Mech.* **544**, 277–307.

HOWE, M. S. 1970 Transmission of an acoustic pulse through a plane vortex sheet. *J. Fluid Mech.* **43**, 353–367.

HOWE, M. S. 1975 Contributions to the theory of aerodynamic sound, with application to excess jet noise and the theory of the flute. *J. Fluid Mech.* **71**, 625–673.

HUBER, P. J. 1981 *Robust Statistics*. Wiley.

JORDAN, P. & COLONIUS, T. 2013 Wave packets and turbulent jet noise. *Annu. Rev. Fluid Mech.* **45**, 173–195.

JORDAN, P. & GERVAIS, Y. 2008 Subsonic jet aeroacoustics: associating experiment, modelling and simulation. *Exp. Fluids* **44** (1), 1–21.

LAUFER, J., SCHLINKER, R. H. & KAPLAN, R. E. 1976 Experiments on supersonic jet noise. *AIAA J.* **14** (4), 489–497.

LEE, M. & BOLTON, J. S. 2007 Source characterization of a subsonic jet by using near-field acoustical holography. *J. Acoust. Soc. Am.* **121** (2), 967–977.

LEE, S.-S. & BRIDGES, J. 2005 Phased-array measurements of single flow hot jets. *AIAA Paper* 2005-2842.

LEIB, S. J. & GOLDSTEIN, M. E. 2011 Hybrid source model for predicting high-speed jet noise. *AIAA J.* **49** (7), 1324–1335.

LIGHTHILL, M. J. 1952 On sound generated aerodynamically. Part 1. General theory. *Proc. R. Soc. Lond.* A **211**, 564–587.

LIGHTHILL, M. J. 1954 On sound generated aerodynamically. Part 2. Turbulence as a source of sound. *Proc. R. Soc. Lond.* A **222**, 1–32.

LILLEY, G. M. 1974 On the noise from jets. *AGARD-CP*-131.

MAESTRELLO, L. & FUNG, Y.-T. 1979 Quasi-periodic structure of a turbulent jet. *J. Sound Vib.* **64** (1), 107–122.

MANI, R. 1976 The influence of jet flow on jet noise. Part 1. The noise of unheated jets. *J. Fluid Mech.* **73**, 753–778.

MANKBADI, R. R. & LIU, J. T. C. 1984 Sound generated aerodynamically revisited: large-scale coherent structures in a turbulent jet as a source of sound. *Proc. R. Soc. Lond.* A **311**, 183–217.

MICHALKE, A. & FUCHS, H. V. 1975 On turbulence and noise of an axisymmetric shear flow. *J. Fluid Mech.* **70**, 179–205.

MORRIS, P. J. & FARASSAT, F. 2002 Acoustic analogy and alternative theories for jet noise prediction. *AIAA J.* **40** (4), 671–680.

OESTREICHER, H. L. 1957 Representation of the field of an acoustic source as a series of multipole fields. *J. Acoust. Soc. Am.* **29** (11), 1219–1222.

PHILLIPS, O. M. 1960 On the generation of sound by supersonic turbulent shear layers. *J. Fluid Mech.* **9**, 1–28.

PRIDMORE-BROWN, D. C. 1958 Sound propagation in a fluid flowing through an attenuating duct. *J. Fluid Mech.* **4**, 399–406.

REBA, R. A., NARAYANAN, S., COLONIUS, T. & SUZUKI, T. 2005 Modeling jet noise from organized structures using near-field hydrodynamic pressure. *AIAA Paper* 2005-3093.

REBA, R. A., SIMONICH, J. C. & SCHLINKER, R. H. 2008 Measurement of source wave-packets in high-speed jets and connection to far-field sound. *AIAA Paper* 2008-2891.

SCHLICHTING, H. 1960 *Boundary-Layer Theory*. McGraw-Hill.

SUPONITSKY, V., SANDHAM, N. D. & MORFEY, C. L. 2010 Linear and nonlinear mechanisms of sound radiation by instability waves in subsonic jets. *J. Fluid Mech.* **658**, 509–538.

SUZUKI, T. 2006 Identification of multipole noise sources in low Mach number jets near the peak frequency. *J. Acoust. Soc. Am.* **119** (6), 3649–3659.

SUZUKI, T. 2010 Review of diagnostic studies on jet-noise sources and generation mechanisms of subsonically-convecting jets. *Fluid Dyn. Res.* **42**, 014001.

SUZUKI, T. 2011 L_1 generalized inverse beam-forming algorithm resolving coherent/incoherent, distributed and multipole sources. *J. Sound Vib.* **330** (24), 5835–5851.

SUZUKI, T. & COLONIUS, T. 2006 Instability waves in a subsonic round jet detected using a near-field phased microphone array. *J. Fluid Mech.* **565**, 197–226.

SUZUKI, T. & LELE, S. K. 2002 Refracted arrival waves in a zone of silence from a finite thickness mixing layer. *J. Acoust. Soc. Am.* **111** (2), 716–728.

SUZUKI, T. & LELE, S. K. 2003 Green's functions for a source in a mixing layer: direct waves, refracted arrival waves and instability waves. *J. Fluid Mech.* **477**, 89–128.

TAM, C. K. W. & AURIAULT, L. 1999 Jet mixing noise from fine-scale turbulence. *AIAA J.* **37** (2), 145–153.

TAM, C. K. W., GOLEBIOWSKI, M. & SEINER, J. M. 1996 Two components of turbulent mixing noise from supersonic jets. *AIAA Paper* 1996-1716.

TAM, C. K. W. & MORRIS, P. J. 1980 The radiation of sound by the instability waves of a compressible plane turbulent shear layer. *J. Fluid Mech.* **98**, 349–381.

TAM, C. K. W., VISWANATHAN, K., AHUJA, K. K. & PANDA, J. 2008 The sources of jet noise: experimental evidence. *J. Fluid Mech.* **615**, 253–292.

TANNA, H. K. 1977 An experimental study of jet noise. Part 1. Turbulent mixing noise. *J. Sound Vib.* **50** (3), 405–428.

TESTER, B. J. & GLEGG, S. A. L. 2008 A review of engine noise source diagnostic methods for static engine tests, with phased arrays and polar correlation techniques. *AIAA Paper* 2008-2854.

TESTER, B. J. & MORFEY, C. L. 1976 Developments in jet noise modelling: theoretical predictions and comparisons with measured data. *J. Sound Vib.* **46** (1), 79–103.

TINNEY, C. E., UKEILEY, L. S. & GLAUSER, M. N. 2008 Low-dimensional characteristics of a transonic jet. Part 2. Estimate and far-field prediction. *J. Fluid Mech.* **615**, 53–92.

UKEILEY, L. S. & PONTON, M. K. 2004 On the near field pressure of a transonic axisymmetric jet. *Intl J. Aeroacoust.* **3** (1), 43–65.

VENKATESH, S. R., POLAK, D. R. & NARAYANAN, S. 2003 Beamforming algorithm for distributed source localization and its application to jet noise. *AIAA J.* **41** (7), 1238–1246.

VISWANATHAN, K. 2004 Aeroacoustics of hot jets. *J. Fluid Mech.* **516**, 39–82.

WUNDROW, D. W. & KHAVARAN, A. 2004 On the applicability of high-frequency approximations to Lilley's equation. *J. Sound Vib.* **272** (3–5), 793–830.